

Trojan resonant dynamics, stability, and chaotic diffusion for parameters relevant to exoplanetary systems

Rocio Isabel Páez

Dip. di Matematica, Università di Roma “Tor Vergata”, Italy
PAEZ@MAT.UNIROMA2.IT

Christos Efthymiopoulos

Research Center for Astronomy and Applied Mathematics, Academy of Athens, Greece
CEFTHIM@ACADEMYOFATHEN.GR

Abstract: The possibility that giant extrasolar planets could have small trojan co-orbital companions has been examined in the literature from both viewpoints of the origin and dynamical stability of such a configuration. Here we aim to investigate the dynamics of hypothetical small trojan exoplanets in domains of secondary resonances embedded within the tadpole domain of motion. To this end, we consider the limit of a massless trojan companion of a giant planet. Without other planets, this is a case of the elliptic restricted three body problem (ERTBP). The presence of additional planets (hereafter referred to as the restricted multi-planet problem, RMPP) induces new direct and indirect secular effects on the dynamics of the trojan body. The paper contains a theoretical and a numerical part. In the theoretical part, we develop a Hamiltonian formalism in action-angle variables, which allows to treat in a unified way resonant dynamics and secular effects on the trojan body in both the ERTBP or the RMPP. In both cases, our formalism leads to a decomposition of the Hamiltonian in two parts, $H = H_b + H_{sec}$. H_b , called the basic model, describes resonant dynamics in the short-period (epicyclic) and synodic (libration) degrees of freedom, while H_{sec} contains only terms depending trigonometrically on slow (secular) angles. H_b is formally identical in the ERTBP and the RMPP, apart from a re-definition of some angular variables. An important physical consequence of this analysis is that the slow chaotic diffusion along resonances proceeds in both the ERTBP and the RMPP by a qualitatively similar dynamical mechanism. We found that this is best approximated by the paradigm of ‘modulational diffusion’. In the paper’s numerical part, we then focus on the ERTBP in order to make a detailed numerical demonstration of the chaotic diffusion process along resonances. Using color stability maps, we first provide a survey of the resonant web for characteristic mass parameter values of the primary, in which the secondary resonances from 1:5 to 1:12 (ratio of the short over the synodic period), as well as their transverse resonant multiplets, appear. We give numerical examples of diffusion of weakly chaotic orbits in the resonant web. We finally make a statistics of the escaping times in the resonant domain, and find power-law tails of the distribution of the escaping times for the slowly diffusing chaotic orbits. Implications of resonant dynamics in the search for trojan exoplanets are discussed.

1 Introduction

A number of studies (Menou and Tabachnik 2003, Dvorak et al. 2004, Érdi and Sándor 2005, Beaugé et al. 2007, Schwarz et al. 2007, Lyra et al. 2009, Cresswell and Nelson 2009, Funk et al. 2012) have pointed toward the hypothesis that small (at most Earth-sized) planets could exist as Trojan companions of giant planets in extrasolar planetary systems. The possibility that pairs of planets might be found in co-orbital resonance in general was first investigated by Laughlin and Chambers (2002). For current and future possibilities to observationally detect extrasolar trojan planets see Giuppone et al. (2012), Haghighipour (2013), Dobrovolskis (2013), and references therein.

In order to ensure that a hypothetical small trojan planet could exist close to a giant planet up to the lifetime of its hosting system, of major interest becomes the question regarding the *long-term stability* of trojan motions in various models of extrasolar planetary systems. Computing the size and form of the domain of stability in the framework of the circular or elliptic restricted three-body problem is a classical problem that has attracted study since decades (see e.g. Rabe 1967, Deprit 1966, Garfinkel 1977, É 1988, Celletti and Giorgilli 1991, Lohinger and Dvorak 1993, Érdi 1997, Giorgilli and Skokos 1997, Gabern et al. 2005, Efthymiopoulos and Sándor 2005, Lhotka et al. 2008, Efthymiopoulos 2013). As exemplified in dynamical studies of Jupiter’s trojan asteroids in our own solar system (Levison et al. 1997, Marzari et al. 2003, Tsiganis et al. 2005, Robutel et al. 2005, Robutel and Gabern 2006, Robutel and Bodossian 2009), a key role in the problem of long term stability is played by the co-existence of various types of *resonances* embedded in the co-orbital domain. Besides the so-called ‘secondary resonances’ (Érdi et al 2007, 2009), i.e. resonances involving the short and long periods of the trojan body (see subsection 2.4 for precise definitions), there are also resonances involving the secular periods of either the trojan body or of its giant companion and/or other giant planets in the same system (see Robutel 2005, Robutel and Gabern 2006). Finally, resonances involving some ‘great inequality’-type motion between the giant planets may occasionally penetrate a trojan swarm, in particular during the early stages of planetary migration (Robutel and Bodossian 2009). The main effect of all these resonant interactions is to produce domains of chaotic diffusion in phase space. Main questions are: i) the geometry and the extent of resonant domains, ii) the speed of chaotic diffusion, and iii) the statistics of the thereby induced times of escape.

Since in observed extrasolar planetary systems gaseous exoplanets appear in an extended range of mass parameters and eccentricities, a parametric study of the effects of resonances on co-orbital dynamics appears necessary. Such a study, aiming to determine the size of the stability domain as a function of the gaseous planet’s mass parameter μ , was performed by Érdi et al. (2007, 2009) in the framework of the elliptic restricted three body problem (ERTBP). These studies practically measure how the size of the main stable domain of the phase space around L_4 and L_5 is affected by the presence of secondary resonances. However, for μ in the range $0.001 \leq \mu \leq 0.01$, we encounter quite *low* order resonances of this type, i.e. resonances of the type 1:n between the short and long period with a relatively small integer n , i.e., $12 \geq n \geq 4$. Hence the phase space volume occupied by the resonances themselves becomes important. Furthermore, as shown in section 3 below, the resonant multiplets formed around a low-order secondary resonance, due to the effects of secular frequencies, consist of groups of resonances whose separation in action space is neither very small (as e.g. for the trojan asteroids in our solar system), nor very big (so as to completely avoid resonance over-

lap). This ‘intermediate’ regime regarding the separation of resonances in a multiplet is due to the fact that, as μ increases, the timescales associated with the three main types of motion, i.e., short-period (of frequency $\mathcal{O}(1)$), long-period (of frequency $\mathcal{O}(\sqrt{\mu})$) and secular (of frequency $\mathcal{O}(\mu_j)$, where μ_j is the mass parameter of the j -th planet in the extrasolar system), no longer separate very well one from the other. This, in turn, complicates the question of characterizing the diffusion within the resonant domain according to well known paradigms of dynamics (e.g. ‘Arnold’, modulational, or resonance overlap (Chirikov) diffusion).

In the present paper, we initiate a parametric study of the resonant structure in the trojan co-orbital domain, as well as of the main types and associated timescales for chaotic diffusion of hypothetical small (considered massless) trojan exoplanets. The paper contains a theoretical and a numerical part. Our numerical study is in the framework of the planar ERTBP. However, in section 2 we introduce a formalism, based on action-angle variables, which renders straightforward generalizations including secular effects of more than one exoplanets. In our study we focus on mass parameters in the range $0.001 \leq \mu \leq 0.006$ for the giant primary. This includes the secondary resonances around the ratios (of the short to long period) from 1:12 to 1:5. For still higher μ (around 0.01) there appear the resonances 1:4 and 1:3, which however, present particularities rendering necessary a separate study (see Deprit 1966, Deprit and Price 1969, Deprit and Henrard 1969, Dullin and Worthington 2013).

The structure of the paper is as follows: section 2 contains theoretical considerations and introduces convenient action-angle variables for our study. We demonstrate that, assuming a multi-planet system far from mean motion resonances, the Hamiltonian can be given the form $H = H_b + H_{sec}$, where: i) H_b , called the ‘basic model’, is a model of two degrees of freedom involving two action-angle pairs that characterize the short period and the synodic motions of the trojan body respectively, ii) H_{sec} contains only ‘slow’ terms, i.e., trigonometric terms depending on secular frequencies. Hence, the dynamics at resonances is approximated as the one due to H_b slowly modulated by the additional influence of H_{sec} . Furthermore, with a re-interpretation of variables, the form of H_b is identical in the RMPP and the ERTBP. Finally, we show how to use these variables in order to compute proper elements for resonant trojan motions. Section 3 is devoted to a parametric study of the stability maps and phase portraits for various values of μ and e' (the eccentricity of the giant primary), in the framework of the ERTBP, in which, our characterization of resonances stems from the general decomposition of the Hamiltonian as in section 2. Using a plane corresponding to our definition of proper elements, we compute and depict the form of the corresponding web or resonances in the plane of proper elements, whereby the volume and relative importance of each resonance can be estimated. Section 4 presents some main types of chaotic diffusion observed by numerically computing orbits with initial conditions in properly chosen chaotic subsets of the resonance web. We provide some criteria to characterize the chaotic diffusion. Finally, we integrate ensembles of orbits and make a statistical study of the escape probabilities as well as the distribution of escape times. Section 5 summarizes the main conclusions of the present study.

2 Theory

2.1 Hamiltonian formalism

The Hamiltonian of the planar ERTBP can be written in heliocentric canonical variables (\mathbf{r}, \mathbf{p}) as:

$$H = \frac{p^2}{2} - \frac{GM}{r} - Gm' \left(\frac{1}{\Delta} - \frac{\mathbf{r} \cdot \mathbf{r}'}{r'^3} \right) \quad (1)$$

where m' is the mass of the primary planet, M the mass of the star, \mathbf{r} , \mathbf{r}' the heliocentric position vectors of the test particle and of the primary respectively, $r = |\mathbf{r}|$, $r' = |\mathbf{r}'|$ and $\Delta = |\mathbf{r} - \mathbf{r}'|$.

The primary's major semi-axis, eccentricity, and argument of the perihelion are denoted by a' , e' , ω' respectively. We set the unit of length as $a' = 1$, and the unit of time such that the mean motion of the primary is equal to $n = 1$. This implies $G(M + m') = 1$. Defining the mass parameter as $\mu = Gm'$, the Hamiltonian in the above units takes the form:

$$H = \frac{p^2}{2} - \frac{1}{r} - \mu \left(\frac{1}{\Delta} - \frac{\mathbf{r} \cdot \mathbf{r}'}{r'^3} - \frac{1}{r} \right) \quad (2)$$

We now introduce modified Delaunay action - angle variables in the above model. As in Brown and Shook (1962; see also Morais 2001), including the small Keplerian correction μ/r in the disturbing function allows to define Delaunay variables with values independent of μ :

$$x = \sqrt{a} - 1, \quad y = \sqrt{a} \left(\sqrt{1 - e^2} - 1 \right) \quad (3)$$

where (a, e) are the major semi-axis and the eccentricity. The action variables (x, y) have the conjugate angles (λ, ω) , i.e. the mean longitude and argument of the perihelion of the trojan (massless) body respectively. The Hamiltonian now reads

$$H = -\frac{1}{2(1+x)^2} - \mu R(\lambda, \omega, x, y, \lambda' = nt; \omega', e', a' = 1) \quad (4)$$

As shown below, in computing proper elements it turns to be crucial to formally remove the explicit dependence of the Hamiltonian on time by introducing a ‘dummy’ action variable I_3 conjugate to λ' , namely

$$H = -\frac{1}{2(1+x)^2} + I_3 - \mu R(\lambda, \omega, x, y, \lambda'; \omega', e') \quad (5)$$

The Hamiltonian (5) represents a system of three degrees of freedom. We now augment the number of degrees of freedom by including the secular effects of additional planets. To this end, assuming that the planets are far from mean motion resonances, it is convenient to approximate the secular dynamics as quasi-periodic, thus introducing a set of secular frequencies, g' for the primary, and g_1, g_2, \dots, g_S for S additional planets. The frequencies $g', g_j, j = 1, \dots, S$ can be computed either by a linear (Laplace) theory, or by a non-linear analytical extension (see, for example, Libert and Sansottera 2013, and references therein), or by purely numerical methods (e.g. frequency analysis, see Laskar 2004). In either case, we adopt the convention that the frequencies g', g_j are the frequencies of the leading terms in

the quasi-periodic representation of the oscillations of the planets' eccentricity vectors. Thus, the time evolution of the latter can be approximated by the equations (see, for example, Morbidelli, 2002, chapter 7)

$$e' \exp i\omega' = e'_0 \exp i(\omega'_0 + g't) + \sum_{k=1}^S A_k \exp i(\omega'_{k0} + g_k t) \quad (6)$$

$$e_j \exp i\omega_j = B_{0j} \exp i(\omega_{0j} + g't) + \sum_{k=1}^S B_{kj} \exp i(\omega'_{kj} + g_k t) \quad (7)$$

Without loss of generality, the constant ω'_0 can be set equal to zero. The positive quantities A_k , B_{kj} , with $k = 1, \dots, S$, and B_0 , are hereafter collectively referred to as 'the amplitudes of oscillation of the planetary eccentricities'. Also, we assume that a typical condition over the solutions (6) holds, namely, that at least for the giant primary one has $e'_0 > \sum_{k=1}^S A_k$. Then, at least the giant primary exhibits a constant, on the average, precession of its eccentricity vector, by the frequency g' , i.e., one can write $e' = e'_0 + F$, $\omega' = g't + G$, where the functions F and G depend trigonometrically on the angles $\phi' = g't$, $\phi_j = g_j t$, $j = 1, \dots, S$, while their size is of the order of the amplitudes A_k , $k = 1, \dots, S$.

For each secular frequency we now introduce a pair of action-angle variables, i.e. the 'dummy' actions I' , I_j and the angles $\phi' = g't$, $\phi_j = g_j t$, $j = 1, 2, \dots, S$. The primary's elements are given by $e' = e'_0 + F(\phi', \phi_j)$, $\omega' = \phi' + G(\phi', \phi_j)$. The form of the Hamiltonian is found by the following steps:

i) Add to the Hamiltonian (5) the direct terms for S planets. The direct term for the j -th planet is:

$$R_{j,direct} = -\mu_j \left(\frac{1}{\Delta_j} - \frac{\mathbf{r} \cdot \mathbf{r}_j}{r_j^3} \right)$$

where $\mu_j = m_j/(M + m')$ with m_j equal to the mass of the j -th planet, and $r_j = |\mathbf{r}_j|$, $\Delta_j = |\mathbf{r} - \mathbf{r}_j|$, \mathbf{r}_j being the heliocentric position vector of the j -th planet. Transcribed to elements, $R_{j,direct}$ depends on $(\lambda, \omega, \lambda_j, \omega_j)$. Assuming that the j -th planet is far from a mean motion resonance with the primary (and hence with the trojan body), we can compute

$$\langle R_{j,direct} \rangle = \frac{1}{4\pi^2} \int_0^{2\pi} \int_0^{2\pi} R_{j,direct} d\lambda d\lambda_j \quad .$$

By rotational symmetry, $\langle R_{j,direct} \rangle$ depends only on the difference $\omega - \omega_j$, and hence, (see Eq.(7)), only on the angles ω , ϕ_j and ϕ_j , $j = 1, 2, \dots, S$. By d'Alembert rules, this implies that it is also of first or higher degree in the eccentricity e_j , i.e., it is of first or higher degree in the amplitudes of oscillation of the planetary eccentricities.

ii) Consider now the indirect effects of the S planets on the trojan body. Again, far from mean motion resonances one has that the primary's major semi-axis remains constant. Then, the indirect effects are accounted for by rendering the parameters e' , ω' in the expression (5) time-dependent (according to Eq.(6)) rather than constants. Replace now $e' = e'_0 + F(\phi', \phi_j)$, $\omega' = \phi' + G(\phi', \phi_j)$ (see above), and Taylor-expand, around e'_0 and ϕ' , assuming F and G small quantities. This leads to:

$$R(\lambda, \omega, x, y, \lambda', \omega', e') = R(\lambda, \omega, x, y, \lambda', \phi'; e'_0) + R_2$$

where R_2 is of degree one or higher in the quantities F, G , and hence, of degree one or higher in the mass parameters μ_j , $j = 1, \dots, S$.

iii) Adding also terms for all dummy actions I', I_j , the final Hamiltonian is now written as

$$H = -\frac{1}{2(1+x)^2} + I_3 + g'I' + \sum_{j=1}^S g_j I_j - \mu R(\lambda, \omega, x, y, \lambda', \phi'; e'_0) - \mu R_2 - \sum_{j=1}^S \mu_j \mathcal{R}_j \quad (8)$$

where R_2 and $\mathcal{R}_j \equiv < R_{j, \text{direct}} >$ contain terms of first or higher degree in the amplitudes of oscillation of the planetary eccentricities.

Two important remarks are in order: i) The function R in Eq. (8) is formally identical to the function R in (5), apart from replacing e' with e'_0 and ω' with ϕ' . ii) The functions R_2 and \mathcal{R}_j , $j = 1, \dots, S$ are of first or higher degree in the amplitudes of oscillation of the planetary eccentricity vectors. These remarks turn to be crucial in the characterization of the diffusion process along resonances in the domain of trojan motion (see below). At any rate, we note that the case where mean motion resonances between the planets are present necessitates a separate treatment, since then the domain of co-orbital motion can be crossed by resonances of the type of the ‘great inequality’ (see Robutel and Gabern 2006).

For studying trojan dynamics, it is important to introduce two new angles, namely $\tau = \lambda - \lambda'$ and $\beta = \omega - \phi'$. The angle τ is the resonant angle corresponding to the 1:1 resonance, with value $\tau = \pi/3$ (at the Lagrangian point L_4). The angle β , on the other hand, expresses the relative position of the pericenter of the trojan body from the pericenter of the primary body, since, one has $\beta = \omega - g't + \mathcal{O}(\mu_j)$. The two angles are formally introduced by defining new canonical variables via the generating function:

$$\mathcal{S}_1 = (\lambda - \lambda')X + \lambda'J_3 + (\omega - \phi')J_2 + \phi'P' + \sum_{j=1}^S \phi_j P_j \quad (9)$$

yielding the transformation to new angles

$$\tau = \lambda - \lambda', \quad q_3 = \lambda', \quad \beta = \omega - \phi', \quad \theta' = \phi', \quad \theta_j = \phi_j, \quad j = 1, \dots, S \quad (10)$$

and new actions X, J_2, J_3, P', P_j connected to the old ones via

$$x = X, \quad I_3 = J_3 - X, \quad y = J_2, \quad I' = P' - J_2, \quad I_j = P_j. \quad (11)$$

Note that preserving the canonical character of the variables requires some modification of the dummy action variables as well. In numerical computations, the transformed dummy variables are employed in the numerical determination of proper element values (see below). Keeping old notation for all variables involved in a identity transformation, we rewrite as $x, \lambda', y, I_j, \phi', \phi_j$ the variables $X = x, q_3 = \lambda', J_2 = y, P_j = I_j, \theta' = \phi', \theta_j = \phi_j$. The Hamiltonian then reads:

$$\begin{aligned} H = & -\frac{1}{2(1+x)^2} - x + J_3 - g'y + g'P' + \sum_{j=1}^S g_j I_j - \mu R(\tau, \beta, x, y, \lambda', \phi'; e'_0) \\ & - \sum_{j=1}^S \mu_j \mathcal{R}_j(x, y, \beta, \phi', \phi_1, \dots, \phi_s) - \mu R_2(x, y, \tau, \beta, \phi', \phi_1, \dots, \phi_s) . \end{aligned}$$

2.2 Forced equilibrium

The Hamiltonian (12) can be recast under the form:

$$H = \langle H \rangle + H_1 \quad (12)$$

where

$$\langle H \rangle = -\frac{1}{2(1+x)^2} - x + J_3 - g'y - \mu \langle R \rangle (\tau, \beta, x, y; e'_0)$$

and

$$H_1 = g'P' + \sum_{j=1}^S g_j I_j - \mu \tilde{R}(\tau, \beta, x, y, \lambda', \phi'; e'_0) - \sum_{j=1}^S \mu_j \mathcal{R}_j(x, y, \beta, \phi', \phi_1, \dots, \phi_s) - \mu R_2(x, y, \tau, \beta, \phi', \phi_1, \dots, \phi_s)$$

with

$$\langle R \rangle = \frac{1}{2\pi} \int_0^{2\pi} R d\lambda', \quad \tilde{R} = R - \langle R \rangle.$$

The exact form of $\langle H \rangle$ up to order two in the eccentricities is given in the Appendix. In the ERTBP, we obtain the same form by replacing β with $\omega - \omega'$ and e'_0 with the (constant) e' , and setting $g' = 0$. Also, it is easy to check that the angle ϕ' does not appear in $\langle H \rangle$ as a consequence of the D'Alembert rules. The action J_3 is an integral of motion under the Hamiltonian flow of $\langle H \rangle$. Thus, the Hamiltonian $\langle H \rangle$ represents a system of two degrees of freedom. We define the forced equilibrium as the solution to the system of equations

$$\dot{\tau} = \frac{\partial \langle H \rangle}{\partial x} = 0, \quad \dot{\beta} = \frac{\partial \langle H \rangle}{\partial y} = 0, \quad \dot{x} = -\frac{\partial \langle H \rangle}{\partial \tau} = 0, \quad \dot{y} = -\frac{\partial \langle H \rangle}{\partial \beta} = 0.$$

For L_4 , one finds that

$$(\tau_0, \beta_0, x_0, y_0) = (\pi/3, \pi/3, 0, \sqrt{1 - e_0'^2} - 1) + O(g') \quad (13)$$

Note that the position of the forced equilibrium, as determined by (13), is time-independent. Nevertheless, the point of Eq. (13) is not an exact equilibrium point under the complete hamiltonian, including the terms \mathcal{R}_j and R_2 . Time-dependent corrections to the position of the forced equilibrium can be determined via a series of canonical transformations, or by working directly with the equations of motion of the complete flow of H (see, for example, Milani 1993, or Morais 2001). Also, Erdi (1997) and Morais (2001) considered corrections to the definition of the forced equilibrium depending on a parameter l , which constitutes a quasi-integral of motion (called 'proper libration'). However, this integral is not precise for the resonant motions considered below. Thus, we do not take such corrections explicitly into account, while corrections depending on a resonant form of the quasi-integral can again be found using canonical transformations on the full Hamiltonian model H .

2.3 Expansion around the forced equilibrium

We will now introduce local action-angle variables around the point of forced equilibrium. The purpose is to characterize the motion by two approximate constants, one of which appears as an action variable (J_s) on the plane (x, τ) around the value (x_0, τ_0) , while the other appears as an action variable (Y_p) on the plane (y, β) around the value (y_0, β_0) . To this end, we first introduce the ‘shift of center’ canonical transformation given by:

$$v = x - x_0, \quad u = \tau - \tau_0, \quad Y = -(W^2 + V^2)/2, \quad \phi = \arctan(V/W) \quad (14)$$

where

$$V = \sqrt{-2y} \sin \beta - \sqrt{-2y_0} \sin \beta_0, \quad W = \sqrt{-2y} \cos \beta - \sqrt{-2y_0} \cos \beta_0 \quad .$$

Re-organising terms, the Hamiltonian (12) takes the form:

$$\begin{aligned} H &= -\frac{1}{2(1+v)^2} - v + J_3 - g'Y \\ &\quad - \mu \left(\mathcal{F}^{(0)}(u, \lambda' - \phi, v, Y; e'_0) + \mathcal{F}^{(1)}(u, \phi, \lambda', v, Y; e'_0) \right) \\ &\quad + g'P' - \mu \mathcal{F}^{(2)}(u, \phi, \lambda', v, Y, \phi'; e'_0) \\ &\quad + \sum_{j=1}^S g_j I_j - \sum_{j=1}^S \mu_j \mathcal{F}_j(u, \phi, v, Y, \phi, \phi', \phi_j, \omega_{0j}, e'_0, e_{0j}) \end{aligned} \quad (15)$$

where (i) $\mathcal{F}^{(0)}$ contains terms depending on the angles λ', ϕ only through the difference $\lambda' - \phi$, (ii) $\mathcal{F}^{(1)}$ contains terms dependent only on non-zero powers of e'_0 and independent of ϕ' , and (iii) $\mathcal{F}^{(2)}$ contains terms dependent on ϕ' and also on non-zero powers of either e'_0 or the oscillation amplitudes of the planetary eccentricities. The above decomposition of the Hamiltonian allows to consider various ‘levels’ of perturbation as follows: We call ‘basic model’ the one of Hamiltonian

$$H_b = -\frac{1}{2(1+v)^2} - v + J_3 - g'Y - \mu \mathcal{F}^{(0)}(u, \lambda' - \phi, v, Y; e'_0) \quad . \quad (16)$$

The total Hamiltonian takes the form $H = H_b + H_{sec}$, where

$$\begin{aligned} H_{sec} &= -\mu \mathcal{F}^{(1)}(u, \phi, \lambda', v, Y; e'_0) + g'P' - \mu \mathcal{F}^{(2)}(u, \phi, \lambda', v, Y, \phi'; e'_0) \\ &\quad + \sum_{j=1}^S g_j I_j - \sum_{j=1}^S \mu_j \mathcal{F}_j(u, \phi, v, Y, \phi, \phi', \phi_j, \omega_{0j}, e'_0, e_{0j}) \quad . \end{aligned}$$

The important remark is, again, that the Hamiltonian H_b is formally identical in the RMPP and in the ERTBP, with the substitution $e'_0 \rightarrow e'$ and setting $g' = 0$. Furthermore, the fact that in (16) the angles λ', ϕ appear only under the combination $\lambda' - \phi$ implies that, in both cases, H_b can be reduced to a system of two degrees of freedom. The reduction is realized by the canonical transformation:

$$\mathcal{S}_2(u, \lambda', \phi, Y_u, Y_s, Y_p) = uY_u + (\lambda' - \phi)Y_f + \phi Y_p \quad (17)$$

yielding

$$\phi_u = \frac{\partial \mathcal{S}_2}{\partial Y_u} = u, \quad \phi_f = \frac{\partial \mathcal{S}_2}{\partial Y_f} = \lambda' - \phi, \quad \phi_p = \frac{\partial \mathcal{S}_2}{\partial Y_p} = \phi,$$

and

$$v = \frac{\partial \mathcal{S}_2}{\partial u} = Y_u, \quad J_3 = \frac{\partial \mathcal{S}_2}{\partial \lambda'} = Y_f, \quad Y = \frac{\partial \mathcal{S}_2}{\partial \phi} = Y_p - Y_f.$$

The subscripts ‘f’ and ‘p’ stand for ‘fast’ and ‘proper’ respectively, for reasons explained below. As before, we keep the old notation for the variables transforming by the identities $\phi_u = u$, $\phi_p = \phi$, and $Y_u = v$. However, it turns to be convenient to retain the new notation for the action $Y_f \equiv J_3$. The Hamiltonian H_b in the new canonical variables reads

$$H_b = -\frac{1}{2(1+v)^2} - v + (1+g')Y_f - g'Y_p - \mu \mathcal{F}^{(0)}(u, \phi_f, v, Y_p - Y_f; e'_0) \quad . \quad (18)$$

Since ϕ is ignorable, Y_p is an integral of the Hamiltonian (18). The physical importance of Y_p can be understood as follows: The action variable Y measures the radial distance from the point of forced equilibrium in the plane (V, W) , in which the forced equilibrium is located at the origin. In a first approximation, the quasi-integral of the proper eccentricity can be defined as

$$e_{p,0} = \sqrt{V^2 + W^2} = \sqrt{-2Y} \quad . \quad (19)$$

However, the above definition neglects the fact that Y is subject to fast variations due to its dependence on Y_f . In fact, by the Hamiltonian equations of motion we readily find that $\dot{Y}_f = \mathcal{O}(\mu)$. The time variation of Y_f is associated to a fast frequency $\dot{\phi}_f = 1 - g$. In fact, by their definition we can see that the variables (ϕ_f, Y_f) describe epicyclic oscillations of the trojan body, i.e. ϕ_f accomplishes one cycle every time when the trojan body passes through a local pericenter. As shown with numerical examples below, the time variations of Y_f become particularly important when one of the following two conditions holds: i) $e'_0 < \mu$, or ii) the orbit of the trojan planet is subject to a low-order resonance. On the other hand, Y_p remains an exact integral of the Hamiltonian (18) even in the cases (i) or (ii), while it is subject only to secular variations in the full Hamiltonian model (15). We thus adopt the following definition of the proper eccentricity:

$$e_p = \sqrt{-2Y_p} \quad . \quad (20)$$

In the Hamiltonian (18), the integral Y_p (or e_p) becomes a label of a system of two degrees of freedom corresponding to the canonical pairs (u, v) and (Y_f, ϕ_f) . Collecting terms from $\mathcal{F}^{(0)}$ linear in Y , we find:

$$\omega_f \equiv \dot{\phi}_f = \frac{\partial H_b}{\partial Y_f} = 1 - 27\mu/8 + g' + \dots, \quad g \equiv \dot{\phi} = \frac{\partial H_b}{\partial Y_p} = 27\mu/8 - g' + \dots \quad (21)$$

We identify ω_f and g as the short-period and secular frequencies, respectively, of the trojan planet. A second averaging over the fast angle ϕ_f yields the Hamiltonian

$$\overline{H_b}(u, v; Y_f, Y_p, e'_0) = -\frac{1}{2(1+v)^2} - v + (1+g')Y_f - g'Y_p - \mu \overline{\mathcal{F}^{(0)}}(u, v, Y_p - Y_f, e'_0) \quad (22)$$

with

$$\overline{\mathcal{F}^{(0)}} = \frac{1}{2\pi} \int_0^{2\pi} \mathcal{F}^{(0)} d\phi_f \quad .$$

The Hamiltonian $\overline{H}_b(u, v; Y_f, Y_p, e'_0)$ represents a system of one degree of freedom, all three quantities Y_f, Y_p, e'_0 serving now as parameters, i.e. constants of motion under the dynamics of \overline{H}_b . The Hamiltonian \overline{H}_b describes the synodic (guiding-center) motions of the trojan planet ¹. The equilibrium point (u_0, v_0) given by

$$\frac{\partial \overline{\mathcal{F}}^{(0)}}{\partial u_0} = \frac{\partial \overline{\mathcal{F}}^{(0)}}{\partial v_0} = 0$$

corresponds to a short-period periodic orbit of the Hamiltonian H_b around the forced equilibrium point. We define the action variable

$$J_s = \frac{1}{2\pi} \int_C (v - v_0) d(u - u_0) \quad (23)$$

where the integration is over a closed invariant curve C around (u_0, v_0) ('s' stands for 'synodic'). The angular variable ϕ_s , conjugate to J_s , evolves in time according to the synodic frequency ω_s given by (see Eq.(31) in subsection 2.5 below)

$$\omega_s = \dot{\phi}_s = \sqrt{\frac{27\mu}{4}} + \dots \quad (24)$$

Figure (1) summarizes the physical meaning of the various action-angle variables introduced so far. We emphasize that in numerical computations one always stays with the original (Cartesian) co-ordinates of the various bodies. Then, translation of the results to action-angle variables and vice-versa is straightforward, passing first to Delaunay elements, and then using the transformations (9, 14, and 17).

2.4 Resonances

The most general form of planar secondary resonances is given by the commensurability relation:

$$m_f \omega_f + m_s \omega_s + m g + m' g' + m_1 g_1 + \dots + m_S g_S = 0 \quad (25)$$

with m_f, m_s, m, m', m_j (with $j = 1, \dots, S$) integers. Of those, the most important are the resonances of the basic Hamiltonian H_b . These resonances exist in the complete spectrum of possible problems, from the planar circular restricted three body problem ($S = 0, g' = 0, e'_0 = 0$) up to the complete multi-planet problem. They are of the form $m_f = 1, m_s < 0, m = 0$, i.e.

$$\omega_f - n \omega_s = 0 \quad (26)$$

with $n = -m_s$. We briefly refer to a resonance of the form (26) as the '1:n' resonance, and to higher order resonances as the $m_f : n$ resonances. For $m_f = 1$ and μ in the range

¹The variables u, v proposed here are similar to the variables X, Y defined in equations (24) or (25) of Beaugé and Roig (2001), via a so-called 'Jupp transformation'. Note, however, the following difference: Our Hamiltonian \overline{H}_b , analogous to Beaugé and Roig's F_0 , is, nevertheless, labeled also by e'_0 (or, simply e' in the ERTBP). Thus, it is *not* the averaged (over fast angles) Hamiltonian of the circular RTBP. From a physical point of view, this expresses the possibility to find an integrable approximation to synodic motions even when $e' \neq 0$. Accordingly, Y_p in our formalism, which is analogous to Beaugé and Roig's W , provides a label for the proper eccentricity rather than simply the eccentricity of the test particle. Again, this expresses the fact that the former, but not the latter, is nearly constant even when $e' \neq 0$.

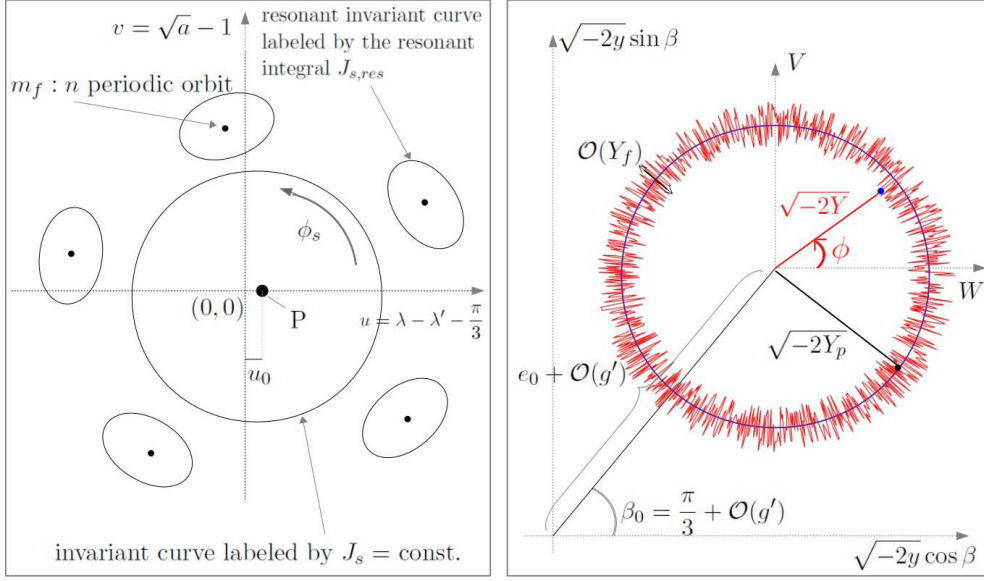


Figure 1: Schematic representation of the physical meaning of the action-angle variables introduced in subsections 2.2. and 2.3. The plane (u, v) corresponds to the ‘synodic’ motion of the trojan body. Under the Hamiltonian H_b , the phase portrait can be represented by a Poincaré surface of section corresponding, e.g., to every time when the angle ϕ_f accomplishes a full cycle. The left panel shows schematically the form of the projection of this section on the plane (u, v) . The central point P represents a stable fixed point corresponding to the short-period periodic orbit around L4. The orbit has frequency ω_f , while its amplitude increases monotonically with Y_f . The forced equilibrium corresponds to $u_0 = 0$, $Y_f = 0$. The point P, however, has in general a shift to positive values $u_0 > 0$ for proper eccentricities larger than zero (see subsection 2.5 below). Far from resonances, the invariant curves around P are labeled by a constant action variable J_s , and its associated angle (phase of the oscillation) ϕ_s . Resonances, and their island chains correspond to rational relations between the frequencies ω_f and ω_s . Within the resonant islands, J_s is no longer preserved, but we have, instead, the preservation of a resonant integral $J_{s,res}$. On the other hand, the plane (W, V) (right panel) depicts the evolution of the trojan body’s eccentricity vector under the Hamiltonian H_b . The motion of the endpoint of the eccentricity vector can be decomposed to a circulation around the forced equilibrium, with angular frequency g , and a fast (of frequency ω_f) ‘in-and-out’ oscillation with respect to a circle of radius e_p , of amplitude which is of order $\mathcal{O}(Y_f)$. Under H_b alone, the quantities Y_p , J_s , or $Y_p, J_{s,res}$ are quasi-integrals for all the regular orbits. Since H_b is formally identical in the ERTBP and in the multi-planet restricted problems, we conclude that the basic features of dynamics induced by H_b apply in the same way with or without additional planets. Furthermore, all extra terms with respect to H_b in the Hamiltonian (12) depend on the slow angles (ϕ, ϕ') and, in the case of the multi-planet problem, ϕ_j , $j = 1, \dots, S$. Thus, all these terms can only slowly modulate the dynamics under H_b . In the case of the ERTBP, the modulation can produce a long-term drift of the values of (Y_p, J_s) , or $Y_p, J_{s,res}$. This is exemplified by numerical simulations in the sequel. The drift can lead to large long term variations of the actions, and eventually to an escape of the trojan body. A similar drift is produced in the multi-planet restricted problem. In the latter case, we have additionally that the position of the forced equilibrium oscillates quasi-periodically around the origin of the (W, V) system of axes. The amplitude of oscillation is of order $\mathcal{O}(\max(\mu_j e_j))$, while the frequency is of first order in the planetary masses.

$0.001 \leq \mu \leq 0.01$, n is in the range $4 \leq n \leq 12$. In the frequency space (ω_f, ω_s, g) , the relations (26) represent planes normal to the plane (ω_f, ω_s) which intersect each other along the g -axis. In the same space, all other resonances with $|m| + |m'| + |m_1| + \dots + |m_S| > 0$ intersect transversally one or more planes of the main resonances. We refer to such resonances as ‘transverse’ if $|m_f| + |n| > 0$, or ‘secular’ if $|m_f| + |n| = 0$. In the numerical examples below, we use the notation (m_f, m_s, m) , for the integers of the resonant condition (25) setting $m' = m_1 = \dots = m_s = 0$ for the case of the ERTBP. As argued above, the dynamical role played by transverse resonances involving the proper frequency g is quite similar to the one played by resonances involving the secular planetary frequencies g' and g_j , $j = 1, \dots, S$. Thus, we do not introduce any further diversification between *transverse* resonances arising in the ERTBP and those due to planetary secular dynamics. This suggests that most numerical results found below regarding the chaotic diffusion at resonances in the case of the ERTBP apply to the transverse resonances of more general models involving more than one disturbing planets.²

2.5 Elliptic restricted three body-problem

In the elliptic planar restricted three body problem we have $S = 0$, $g' = 0$, $e' = e'_0 = \text{const.}$. Then, $\beta \equiv \omega$, and $v \equiv x$. the Hamiltonian (15) takes the form:

$$H_{ell} = -\frac{1}{2(1+x)^2} - x + Y_f - \mu \left(\mathcal{F}^{(0)}(u, \phi_f, x, Y_p - Y_f, e') + \mathcal{F}^{(1)}(u, \phi_f, \phi, x, Y_p - Y_f, e') \right) \quad (27)$$

The function $\mathcal{F}^{(1)}$ contains terms of at least first order in e' . Hence, $\dot{Y}_p = \mathcal{O}(e')$. This implies that Y_p (or e_p) remains a good quasi-integral for not very high values of the primary’s eccentricity. On the other hand, a more accurate ($\mathcal{O}(e'^2)$) quasi-integral can be computed by a first order adiabatic theory.

The form of the functions $\mathcal{F}^{(0)}$ and $\mathcal{F}^{(1)}$, with an error $\mathcal{O}(x) \approx \mathcal{O}(\mu^{1/2})$, is given in the Appendix. From this we deduce the shift in position, with respect to L4, of the fixed point of $\mathcal{F}^{(0)}$, corresponding to the short-period orbit around L4 (Namouni and Murray 2000). The shift is given by $u_0 = \tau_0 - \pi/3$, where τ_0 is the solution of $\partial \mathcal{F}^{(0)} / \partial \tau_0 = 0$. We find:

$$u_0 = \frac{29\sqrt{3}}{24} e_p^2 + \dots \quad (28)$$

²A comparison between the terminology for resonances employed here and in Robutel and Gabern (2006, referring to the case of Jupiter’s trojan asteroids), is in order. Robutel and Gabern distinguish four ‘families’ of resonances. Two of these, however, (Family II and IV) involve the frequencies $\nu_{1,2} = 2n_{\text{Saturn}} - n_{\text{Jupiter}}$ and $\nu_{2,5} = 5n_{\text{Saturn}} - 2n_{\text{Jupiter}}$, which, due to the Great Inequality, both play an important role in the dynamics of Jupiter’s trojan swarm. Also, Family III involves the asteroids’ secular frequency s , thus it applies only to inclined motions. Here we consider systems with a rather planar geometry and far from mean motion resonances, for which only Family I-type resonances of Robutel and Gabern are relevant. Their ν corresponds to our synodic frequency ω_s . Also, they use n_5 (the mean motion of Jupiter = 1 in our units), while we use $\omega_f = n_5 - g = 1 - g$, which, as explained above, is the frequency of epicyclic oscillations of the trojan body. Thus, The Family I of Robutel and Gabern corresponds to our definition (25) if we set $m_f = -1$, $m_s \equiv p$, $m \equiv q - 1$, $m' \equiv q_5$, $m_1 \equiv q_6$. We emphasize, however, that due to the particular values of the frequencies for the Trojan swarm, Family I of Robutel and Gabern has the restrictions $m_f = -1$, $m + m' + m_1 = 0$. On the contrary, such restriction is not present in our computations. On the other hand, our ‘secular’ resonances require both m_s and m_f to be equal to zero. Thus, from a dynamical point of view, they are qualitatively closer to their Family III.

where the error is of order 4 in the eccentricities e_p, e' . Taylor-expanding $\overline{H}_{b,ell}$ (Eq.(22), for the ERTBP) around u_0 up to terms of second degree in $\delta u = u - u_0$, we find (up to terms of first order in μ and second order in the eccentricities):

$$\begin{aligned} \overline{H}_{b,ell} = & -\frac{1}{2} + Y_f - \mu \left(\frac{27}{8} + \dots \right) \frac{e_{p,0}^2}{2} \\ & - \frac{3}{2}x^2 + \dots - \mu \left(\frac{9}{8} + \frac{63e'^2}{16} + \frac{129e_{p,0}^2}{64} + \dots \right) \delta u^2 + \dots \end{aligned} \quad (29)$$

where $\frac{e_{p,0}^2}{2} = -Y_p + Y_f$. Since Y_f is $\mathcal{O}(\mu)$, up to terms linear in μ the part

$$H_{syn} = -\frac{3}{2}x^2 - \mu \left(\frac{9}{8} + \frac{63e'^2}{16} + \frac{129e_p^2}{64} + \dots \right) \delta u^2 \quad (30)$$

defines a harmonic oscillator for the synodic degree of freedom. The corresponding synodic frequency is

$$\omega_s = \sqrt{6\mu \left(\frac{9}{8} + \frac{63e'^2}{16} + \frac{129e_p^2}{64} + \dots \right)} . \quad (31)$$

On the other hand, the secular frequency is given by $g = \partial \overline{H}_{b,ell} / \partial Y_p$. Assuming a harmonic solution $\delta u = \delta u_0 \cos(\omega_s t + \phi_{0s})$, and averaging over the synodic period $\langle \delta u^2 \rangle = \delta u_0^2 / 2$, we find

$$g = \mu \left(\frac{27}{8} + \frac{129}{64} \delta u_0^2 + \dots \right) . \quad (32)$$

Eq.(32) applies for orbits in the neighborhood of the short period orbit. A resonant periodic orbit $m_f : n$ bifurcates from the short-period orbit at $\delta u = 0$ provided that

$$m_f \left(1 - \frac{27\mu}{8} + \dots \right) = n \sqrt{6\mu \left(\frac{9}{8} + \frac{63e'^2}{16} + \frac{129e_p^2}{64} + \dots \right)} . \quad (33)$$

Such orbits appear in pairs, one stable and one unstable, and it is well known that they form ‘bridges’ connecting a short period with a long period orbit (Deprit and Rabe, 1968). Under the full Hamiltonian dynamics of H_{ell} , the bifurcation generates a 2D-torus, which is the product of the above orbit times a circle on the plane W, V with frequency $g = 27\mu/8$.

Under the Hamiltonian flow of H_b , a $m_f : n$ resonant periodic orbit forms n fixed points on a surface of section (u, x) , for $\text{mod}(\phi_f, 2\pi) = \text{const}$. Around the fixed points of a stable resonant periodic orbit there are formed islands of stability (see figure 1, schematic), surrounded by separatrix-like thin chaotic layers formed around the unstable fixed points. Beyond the bifurcation point, as e_p increases, the fixed points move outwards, i.e., at larger distances from the central fixed point $(x, u) = (0, u_0)$, while the resonant islands of stability grow in size. The growth is faster for lower-order resonant periodic orbits (i.e. for smaller n). This growth, however, stops when the islands of stability enter in the main chaotic sea around the tadpole domain of stability. Numerically computed examples of this behavior are given in section 3 below.

2.6 Modulational diffusion

The resonant periodic orbits arising under the flow of H_b correspond to resonant 2D tube tori under the flow of the full model H_{ell} . Respectively, the resonant fixed points correspond to one-dimensional tori on a surface of section $\text{mod}(\phi_f, 2\pi) = \text{const.}$ Projected on the plane (u, x) , these tori appear as thick curves (see Fig.2 below). In the same projection, the islands of stability and their delimiting separatrix-like chaotic layers are observed to undergo ‘pulsations’, i.e. some periodic shift in the plane (u, x) modulated at the frequency g and its multiples. Such pulsation is induced by the presence (in H_{ell} but not in H_b) of terms trigonometric in the angle ϕ and its multiples.

The modulation of all resonant motions by slow trigonometric terms results in a long-term chaotic diffusion taking place in the space of the action variables (J_s, Y_p) . In fact, based on the pulsation width of the separatrices, we encounter the following two diffusion regimes:

i) *Non-overlapping resonances*: for small pulsation widths, the separatrices of one resonance do not enter to the pulsation domain of the separatrices of nearby resonances. In such cases the rate of the chaotic diffusion is quite small, and the diffusion becomes practically undetectable. Also, the geometry of resonances in the action space is closer to the paradigm of Arnold diffusion (Arnold 1964). An example of chaotic orbit in such regime is given in section 4 below.

ii) *Partially-overlapping resonances*: for large pulsation widths, the pulsation domains of more than one separatrices of nearby resonances partially overlap. In this case the rate of chaotic diffusion increases dramatically. As shown in section 4, the chaotic orbits in the most prominent chaotic layers exhibit a diffusion timescale of the order of 1Myr. The diffusion leads to final escapes from the resonant domain and from the overall tadpole domain. However, there is also a weakly chaotic population exhibiting long times of stickiness, with a power-law distribution of the stickiness times characteristic of long-term correlated chaotic motions (see Meiss 1992, p. 843, and references therein, also Ding et al. 1990, Cheng et al. 1992). At any rate, in most cases we find that the overlapping of resonances is not complete, as is, for example, the case of resonant multiplets for Jupiter’s trojan asteroids (see Robutel and Gabern 2006). As a result, the overall diffusion process in our experiments is closer to the paradigm of *modulational* diffusion (Chirikov et al. 1985). Finally, there are regular resonant orbits that never escape the system.

Figure 2 gives a typical example of the modulational diffusion regime. The panel (a) shows a ‘pericentric’ surface of section (u, x) (precise definition given in section 3 below) which depicts the structure of the phase space in the circular model ($e' = 0$ for the dynamics under the Hamiltonian H_b), when $\mu = 0.0041$, $e_p = 0.01675$. For these parameters, the phase portrait is dominated by the islands of the 1:6 resonance. The separatrix-like chaotic layers surrounding the resonance are very thin, while the resonant islands are delimited by both inner and outer librational KAM curves. Thus, all orbits inside this resonance cannot communicate with orbits of nearby resonances embedded either in the remaining part of the stability domain or in the chaotic sea surrounding the stability domain. An orbit near the separatrix layer of the 1 : 6 resonance is shown in blue in Fig.2a. Note that $e_p = \sqrt{-2Y_p}$ is an exact integral of motion of the flow under H_b , as confirmed by a numerical computation of e_p (Fig.2c, black curve). On the contrary, the distance $(W^2 + V^2)^{1/2}$ from the forced equilibrium which coincides with the osculating value of the eccentricity e (Fig.2c, blue curve) undergoes substantial short-period oscillations (of order $O(\mu)$). Thus, e_p as defined via Eq. (20) is a

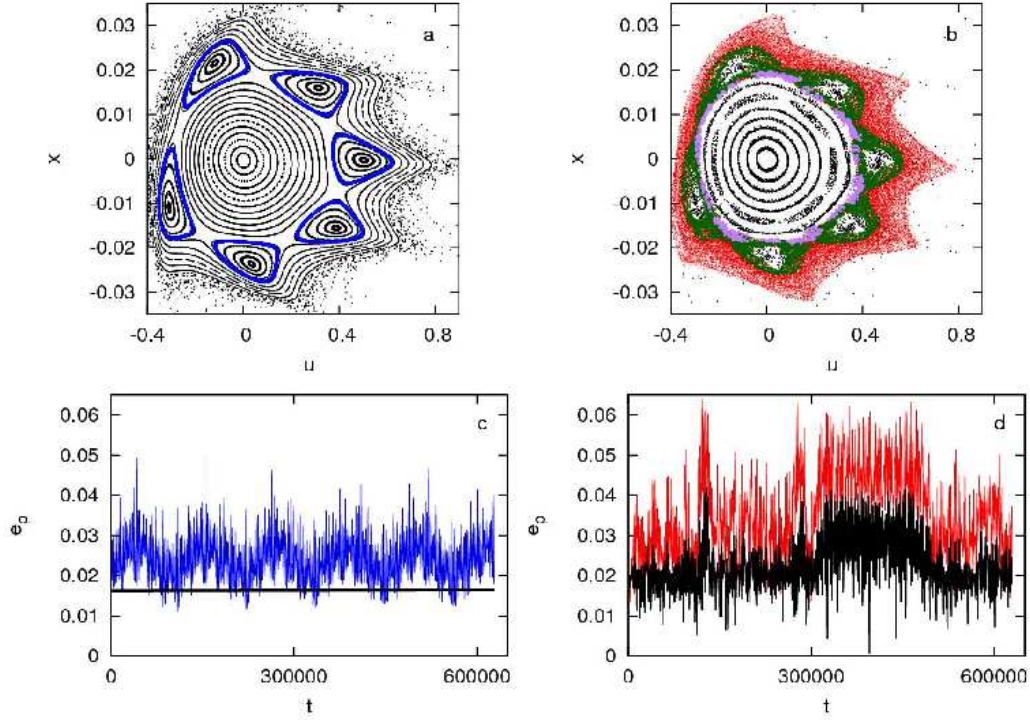


Figure 2: (a) - Phase portrait (pericenter surface of section) in the variables u, x , when $\mu = 0.0041$, $e_p = 0.01675$, $e' = 0$ (circular case). A orbit moving in the thin separatrix layer of the $1 : 6$ resonance is shown in blue (with initial condition $x = 0$, $u = 0.376$). (b) - Same as in (a) but now in the elliptic case $e' = 0.02$. The chaotic orbit moves in the separatrix layer of the $1 : 6$ resonance up to a time 10^4 (green), but later it expands towards the chaotic layers of other adjacent resonances (red). (c) Time evolution of e_p (Eq. (20), black curve) and $e_{p,0}$ (Eq. (19), blue curve), for the blue orbit of (a). (d) - Time evolution of e_p (black) and $e_{p,0}$ (red) for the coloured chaotic orbit of (b).

much better measure of the proper eccentricity than the usual definition $(W^2 + V^2)^{1/2}$.

Figure 2b, now, shows the projection on the plane (u, x) of a 4D pericentric surface of section in the elliptic case, when $e' = 0.02$ (black points), on which we superpose in colors the points of *one* chaotic orbit undergoing modulated diffusion. The 1:6 resonance is still clearly visible on the (u, x) projection, giving rise to six islands, one of which intersects the line $x = 0$ at values around $u \approx 0.4$. Another smaller 6-island chain, intersecting the line $x = 0$ at about $u \approx 0.3$ is also distinguishable. As shown in section 4, the latter corresponds to the transverse resonance $(1, -6, -1)$, whose extent, however is limited and produces no substantial overlapping with other low order resonances. On the other hand, the pulsation of the separatrix of the 1:6 resonance does results in a substantial overlapping of this resonance with other outer resonances surrounding the origin. As a result, an orbit started in the separatrix layer of the 1:6 resonance later communicates with the separatrix layers of the outer resonances. In the example of Fig.2b, the orbit with initial conditions indicated in the caption remains confined in the neighborhood of the 1:6 resonance up to a time $\sim 2\pi \times 10^4$ (green points), while at later times (up to $\sim 2\pi \times 10^5$) the same orbit expands to embed several higher order resonances of the form $m_f : n$ as well as some transverse resonances of the elliptic problem. A careful inspection shows that the orbit undergoes several outward and inward motions in the whole domain from the 1:6 resonance up to the outer resonances, while the orbit eventually escapes from the system at still larger times (of order 10^6). The various outward or inward transitions are abrupt, and they are marked by corresponding transitions in the value of e_p , which is now only an approximate adiabatic invariant. Such transitions are shown in Fig.2d (black curve). Here, an overall comparison with the time evolution of the quantity $(W^2 + V^2)^{1/2}$ (red curve), shows that the definition of e_p via the action variable Y_p still yields a useful measure of the proper eccentricity, while $(W^2 + V^2)^{1/2}$ presents wild variations even in short timescales. In fact, the time behavior of e_p presents jumps at all outward or inward transitions of the corresponding orbit of Fig.2b. A further analysis of how the diffusion progresses in the space of action variables (J_s, Y_p) is given in section 4.

3 Stability Maps and resonant structures

The present section contains a survey of the resonant structures appearing in the space of proper elements (J_s, Y_p) for an ensemble of parameter values (μ, e') representative of cases in which a resonance of the form $1 : n$, with $n = 5, \dots, 12$, and its associated multiplets, dominates in phase space. A survey of phase portraits allows to define a proper set of initial conditions choosen in a grid providing a convenient representation of the action variables (J_s, Y_p) . An atlas of stability maps are then computed by means of a suitable chaotic indicator.

3.1 Phase portraits and choice of initial conditions

Phase portraits are visualized by means of appropriate Poincaré surfaces of section. In numerical experiments, it turns practical to consider *apsidal* sections, in which the orbits pass through consecutive local pericentric or apocentric positions. Here we adopt the pericenter crossing condition, $\dot{r} = 0$ and $\ddot{r} > 0$, where \dot{r} is the radial velocity in the heliocentric frame.

The pericentric surface of section is two-dimensional if $e' = 0$, and four-dimensional if $e' > 0$. In the former case, the term $\mathcal{F}^{(1)}$ in the Hamiltonian (27) becomes equal to zero by identity. The exact invariance of Y_p is equivalent to the exact invariance of the Jacobi

constant C_J in the barycentric rotating frame. In practice, it is more convenient to construct surfaces of section of constant values of C_J rather than Y_p . Yet, we label these surfaces of section using a corresponding value of $e_p = \sqrt{-2Y_p}$. This correspondance is established as follows: to a given value of Y_p corresponds a short-period orbit crossing the surface of section at a fixed point with coordinate u_0 given by Eq.(28) with $e_p = \sqrt{-2Y_p}$ (Eq.(20)). Noticing that, for $e' = 0$ the angles ϕ and ω coincide, i.e. $\phi_f = \lambda' - \omega$, the remaining initial conditions of the fixed point are given by

$$x_0 = 0, \quad \phi_{f,0} = \lambda' - \omega_0 = -u_0 - \frac{\pi}{3}, \quad Y_f = 0 \quad . \quad (34)$$

The condition on ϕ_f is the pericenter crossing condition. Setting the Delaunay action y_0 as $y = Y_p - Y_f = Y_p$, and the angle $\lambda_0 = \lambda' + \pi/3 + u_0$, with $\lambda' = 0$ at $t = 0$, one then has all four values of the Delaunay variables $(\lambda_0, \omega_0, x_0, y_0)$, whereby cartesian position and velocity vectors can be computed. This allows to compute the Jacobi constant C_{J0} corresponding to the short-period orbit of given e_p . We refer to the whole surface of section with $C_J = C_{J0}$ as the section corresponding to a ‘given value of e_p ’ (referred to as ‘the proper eccentricity’), although, for fixed C_J , e_p actually changes somewhat as we move on the section away from the point (u_0, x_0) . Now, for any other point (u, x) on the surface of section, the pericentric condition yields $\omega = u + \pi/3$, while y (and hence the precise value of Y_p) can be computed by solving numerically the Jacobi-constant equation $C_J = C_{J0}$.

We produce surface of section plots taking 35 equispaced initial pericentric conditions along a fixed line of the form $x = B(u - u_0)$, up to $u = 1.0$, and solving always the equation $C_J = C_{J0}$. The inclination B is determined according to a rule explained below. For each initial condition, we integrate the orbits and collect 1000 successive points on the surface of section, plotted in the plane (u, x) .

Repeating this process for different values of μ , from 0.001 to 0.01, with an interval of $\Delta\mu = 0.001$, and with $e_p = 0$, allows to explore the whole range of values containing the resonances of the form 1:n, with $4 \leq n \leq 12$. In particular, between $\mu = 0.0012$ and $\mu = 0.0056$ we find the resonances for $n = 12, 11, \dots, 5$. Higher order resonances of the form 2:(2n+1), 3:(3n+1) or 3:(3n+2), etc., are also distinguishable by simple visual inspection.

An example is shown in Figure 3. The plots for $\mu = 0.0031$ (lower row) and $\mu = 0.0041$ (upper row) correspond to the pericentric Poincaré surfaces of section in two cases where the resonances 1:7 and 1:6, respectively, are conspicuous in phase space. We note that one of the fixed points of the stable periodic orbit corresponding to the 1:6 resonance lies on the horizontal line $x = 0$. This is so for all even resonances (i.e. 1 : n with n even). On the other hand, for odd resonances (1 : n with n odd) all stable fixed points lie on lines of the form $x = B(u - u_0)$ with $B \neq 0$. In our numerical study of FLI maps, we use the following slopes computed numerically by inspecting surfaces of sections similar to Fig.3:

Resonance	μ	slope B
1:11	0.0014	0.04
1:9	0.0021	0.025
1:7	0.0031	0.015
1:5	0.0056	0.03

A resonant periodic orbit 1:n bifurcates from the central short-period orbit at pairs of values (μ, e_p) satisfying Eq.(33). As shown in Fig.3, for fixed μ , the resonant orbits move

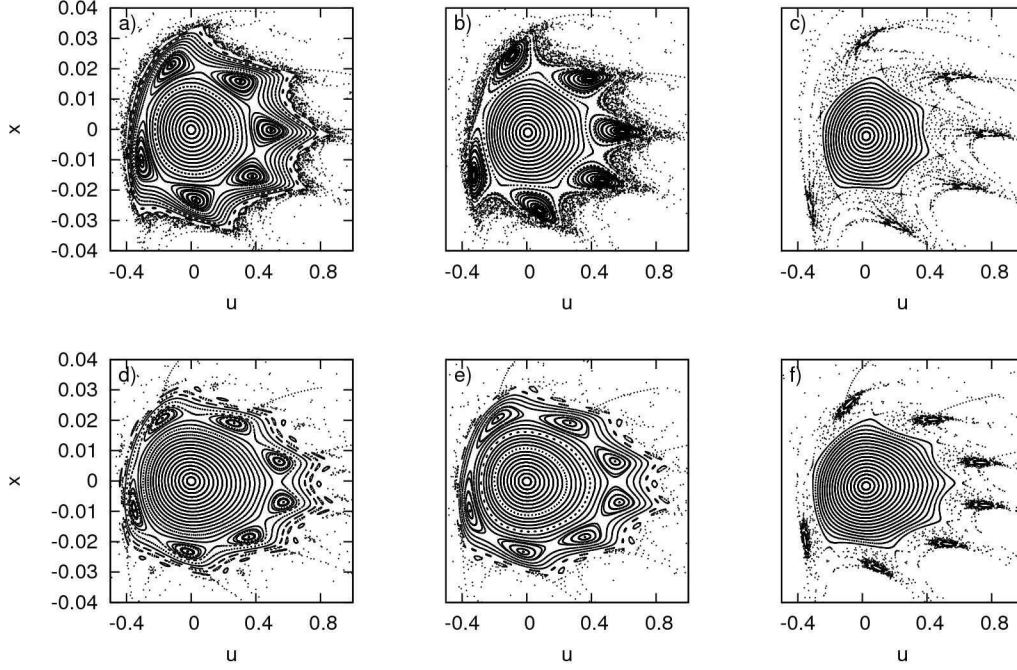


Figure 3: Surface of section in the circular case ($e' = 0$) for $\mu = 0.0041$ (upper plots) and $\mu = 0.0031$ (lower plots). The values of e_p are, in each case: $e_p = 0.0001$ (a), $e_p = 0.06$ (b), $e_p = 0.1$ (c), $e_p = 0.0001$ (d), $e_p = 0.05$ (e) and $e_p = 0.1$ (f).

outwards as e_p increases, while their corresponding island chains grow in size. The three panels in each row of Fig.3 correspond to three different values of e_p (see caption), in increasing value from left to right. For small values of e_p , the stability islands in both cases are surrounded by invariant tori. The stability domain around (u_0, x_0) extends from $u \simeq -0.4$ to $u \simeq 0.8$, for $x = 0$. Some small higher order resonances are visible at the border of the stability domain. However, as e_p increases, the resonant islands grow in size, while most of their surrounding invariant tori are destroyed. For a critical value of e_p , the last KAM torus surrounding the resonant island chain is destroyed. We find that this value satisfies $e_{p,crit} < 0.1$ in all studied cases. For $e_p > e_{p,crit}$, the resonant islands are surrounded by the outer chaotic sea, which penetrates the stability domain closer and closer to the center. Thus, for $e_p = 0.08$ the right boundary of the stability domain shrinks to $u = 0.4$ or less.

Similar phenomena appear if e_p is kept fixed while varying μ . As μ increases beyond the bifurcation value, the stability islands of the resonance move outwards and increase in size. Reaching a certain critical value of μ , the last invariant torus at the border of stability surrounding the islands is destroyed. This mechanism also shrinks the stability region, although by abrupt steps. On the other hand, different values of μ give rise to different resonances. Thus, the size of the domain of stability undergoes abrupt variations connected to the bifurcations of new resonances (see Erdi et al. 2007 for a quantitative study of this effect in the case $e_p = 0$).

3.2 FLI stability maps

When $e' > 0$ the pericentric surface of section becomes 4-dimensional. Then, projection effects on the plane (u, x) render unclear a detailed visualization of the resonant structures (cf. Fig.2b). Nevertheless, a convenient visualization is possible in the space of the actions (J_s, Y_p) . In practice, we demonstrate all results in a space of proper elements Δu (libration angle) and e_p (proper eccentricity), which are in one to one relation with the action variables (J_s, Y_p) . The quantity Δu is defined as follows: for given e_p , we first determine u_0 via Eq.(28). Then, we consider all invariant curves around the equilibrium point $(u = u_0, x = 0)$ of the one degree of freedom Hamiltonian \overline{H}_b (Eq.(22)), as well as a line of initial conditions $x = B(u - u_0)$, where, in all examples below, $B = 0$ for even resonances, or as indicated in the table for odd resonances. We call u_p the point where the invariant curve corresponding to the action value J_s intersects the above line of initial conditions. Finally, we set $\Delta u = u_p - u_0$. Using the harmonic oscillator approximation of Eq.(30), the action J_s can be approximated as $J_s = E_s/\omega_s$, where ω_s is given by Eq.(31), while E_s is the oscillator energy $E_s = -H_{syn}$ found by substituting the initial conditions to Eq.(30). Then, up to quadratic terms in Δu , one has

$$J_s = \frac{3B^2/2 + \mu(9/8 + 63e'^2/16 + 129e_p^2/64)}{[6\mu(9/8 + 63e'^2/16 + 129e_p^2/64)]^{1/2}} \Delta u^2 + \mathcal{O}(\Delta u^4) \quad (35)$$

Note that for odd resonances, Δu is *not* equal to the half-width D_p of the oscillation of the variable u along the invariant curve of \overline{H}_b corresponding to the action variable J_s , which is used as a standard definition of the proper libration angle. Instead, locating the point where the ellipse defined by $E_s = -H_{syn}$ intersects the axis $x = 0$, we find

$$D_p = \left[\frac{3B^2/2 + \mu(9/8 + 63e'^2/16 + 129e_p^2/64)}{\mu(9/8 + 63e'^2/16 + 129e_p^2/64)} \right]^{1/2} \Delta u + \mathcal{O}(\Delta u^2) \quad (36)$$

In numerical simulations, after fixing μ and e' , we chose a 400×400 grid of initial conditions in the square $0 \leq \Delta u \leq 1$, $0 \leq e_p \leq 0.1$, setting also $x = B\Delta u$ and $y = Y_p + Y_f$ with $Y_f = 0$, $\phi_f = -\pi/3$, $\phi = \pi/3$. This completely specifies all Delaunay variables for one orbit, and hence its initial cartesian position and velocity vectors as well as the value of the dummy action $I_3 = 0$ in the Hamiltonian (5). Finally, we express (5) in the original Cartesian form

$$E = H \equiv \frac{p^2}{2} + I_3 - \frac{1}{r} - \mu \left(\frac{1}{\Delta} - \frac{\mathbf{r} \cdot \mathbf{r}'}{r'^3} - \frac{1}{r} \right) \quad (37)$$

and keep track of the constancy of the numerical value of the energy E as a probe of the accuracy of numerical integrations.

Stability maps are computed over the above grid of initial conditions by means of color-scaled plots of the value of a suitable chaotic indicator. Here we employ the Fast Lyapunov Indicator (FLI, see Froeschlé et al. 2000) given by

$$\Psi(t) = \sup_t \log_{10}(\|\xi\|),$$

where ξ is the variational (deviation) vector computed by solving the variational equations of motion along with the orbital equations of motion and $\|\cdot\|$ denotes the L_2 norm. For

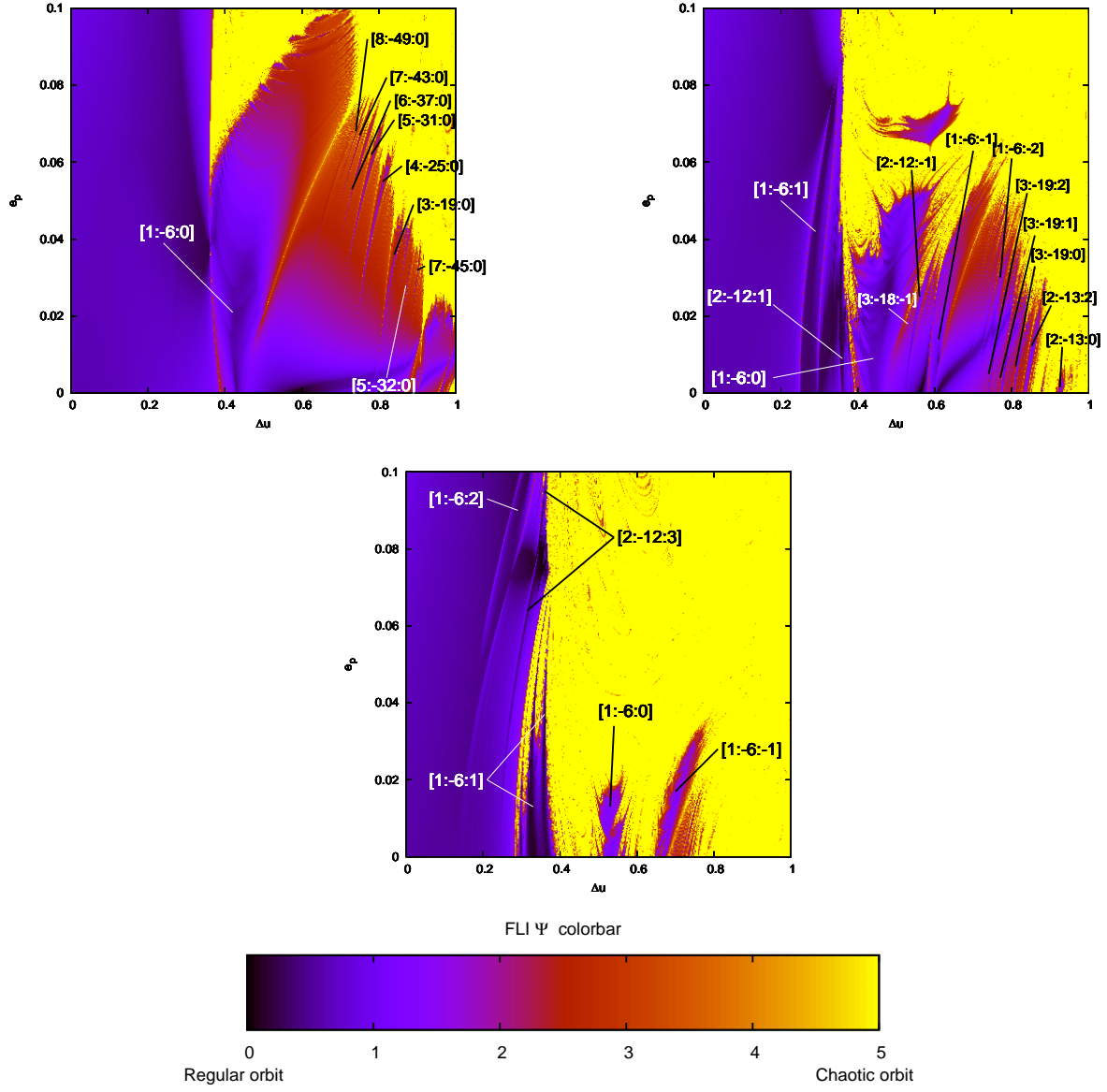


Figure 4: FLI maps with details of the resonances, for $e' = 0$ (left upper panel), $e' = 0.02$ (right upper panel) and $e' = 0.06$ (lower panel).

computing FLIs we implement a 7th-8th order Runge-Kutta method, with a timestep equal to $1/300$ of the period of the primary ($= 2\pi$ in our units). In order to avoid numerical overflows, we stop integrating orbits that have clearly reached escape. The latter are identified by a sudden jump of the energy error to levels beyond 10^{-4} , while for non-escaping orbits the energy error at 10^3 periods is less than 10^{-9} . Also, we stop integrating the variational equations of orbits reaching FLI values larger than 50.

Figure 4 shows an example of computed stability maps for $\mu = 0.0041$ and three values of e' , namely $e' = 0$, $e' = 0.02$, and $e' = 0.06$. In each plot, the value of Ψ is given in a color scale for all 400×400 grid initial conditions in the plane of proper elements $(\Delta u, e_p)$. The color scale was set in the range $0 \leq \Psi \leq 5$. Regular orbits correspond to darker colors (black) representing low values of Ψ , while the most chaotic orbits correspond to light colors (yellow). Orbits with $\Psi > 5$ are shown also in yellow.

A more detailed resonance identification was made by means of frequency analysis (Laskar 1990). The most conspicuous resonances are explicitly indicated in all three plots. For $e' = 0$ (top left panel), the resonance 1:6 dominates the stability map. Besides, several resonances of the type $(m, -6m + 1, 0)$ produce strips penetrating the stability domain. In agreement with what was shown in the surface of section plots of Fig.3, the width of the 1:6 resonance increases, initially, as e_p increases from zero up to a value $e_p \sim 0.06$. Also, the chaotic separatrix-like layers around the resonance remain thin. However, for $e_p > 0.06$ the resonance is detached from the main stability domain. Then, its corresponding islands of stability are embedded in a chaotic sea corresponding to orbits with a fast escape. For still larger e_p (around 0.1) the central periodic orbit becomes unstable and the corresponding islands disappear. In general, this, as well as all higher order resonances move outwards (towards higher values of Δu) as e_p increases. Thus, all resonant strips have a small positive slope in Fig.4.

On the other hand, increasing the value of e' causes new *transverse* resonances to appear. For $e' = 0.02$ (top right panel), resonances of the form $(n, -6n, m)$, or $(n, -6n - 1, m)$, with $n = 1, 2, 3$ and $m = -2$ up to $m = 2$ are distinguishable. We note that in general the angle formed between the transverse resonances ($m \neq 0$) and the secondary resonances of the circular problem ($m = 0$) is small (of order g/ω_s), where g and ω_s are the respective secular and synodic frequencies. This small transversality implies that the intersection point of most mutually transverse resonances lies in the chaotic zone, i.e. far from the domain of stability. In particular, the transverse resonances with $m > 0$ have no intersection with the main resonance 1:6 inside the stability domain. In fact, these transverse resonances penetrate the domain of stability in isolated, single-resonance strips, along which the orbits undergo weakly chaotic diffusion that bears many features of Arnold diffusion as also shown in Robutel and Gabern (2006). On the other hand, the resonances that are beyond the border of the inner stability domain form multiplets, in which it has already been argued that the chaotic diffusion has features of modulational diffusion. This gives a mechanism of efficient escape for chaotic orbits (see section 4).

For still higher values of e' (Fig.4, down panel for $e' = 0.06$), new transversal resonances appear. In fact, as e' increases all transverse resonances move in the direction from top left to bottom right, until reaching large values of Δu , after which they enter into the main chaotic sea surrounding the domain of stability. Then, they become less significant.

3.3 Survey of resonances

Figures 5 to 12, show a surveys of the resonances, as depicted by numerically computed FLI maps, for different cases of e' , and for the mass parameters $\mu = 0.0012, 0.0014, 0.0016, 0.0021, 0.0024, 0.0031, 0.0041$ and 0.0056 . These are representative of the multiplets formed around the resonances 1:5, 1:6, 1:7, 1:8, 1:9, 1:10, 1:11 and 1:12, respectively. In each plot, the values for e' are 0, 0.02, 0.04, 0.06, 0.08 and 0.1, from top to bottom and left to right. Inspecting these plots, we emphasize the following features:

i) The size of the non-resonant domain does not change much with variations of e' . In fact, in all these plots we observe that, despite the fact that as e' evolves new transversal resonances appear, the non-resonant domain keeps its limits nearly constant (at about 0.2 in Fig 5, 0.3 in Fig 6, 0.4 in Fig 7, 0.45 in Fig 8 and Fig 9, 0.6 in Fig 10, 0.35 in Fig 11 and 0.7 in Fig 12). On the other hand, the resonant domain, which for low (but non-zero) values of e' is filled with small transverse resonances, gradually shrinks within the chaotic sea, and for values of e' around 0.1, it completely disappears. This gives a natural limit for the values of e' to consider, since no important resonances survive for $e' > 0.1$.

ii) Around a main resonance, we identify new emerging transverse resonances, of the kind $(1, -n, m)$, with m a small integer. Since they are triple resonances with commensurability with g , they are not present for $e' = 0$, but for greater values they become evident, especially some isolated ones which penetrate inside the non-resonant region. As e' increases, the whole structure moves outwards (towards increasing values of Δu) and also downwards (towards smaller values of e_p). For bigger values of e' , the main resonances 1:n generally disappear or they are small, leaving space for transverse resonances to dominate in action space.

iii) Finally, in some plots (as in Fig. 5, 6, 7, 11), we can see traces, appearing as thin darker lines in the chaotic domain, of the stable invariant manifolds emanating from lower-dimensional invariant objects around L_3 , such as the short-period planar Lyapunov orbits in the case $e' = 0$, or their associated 2D-tori, for $e' = 0$. Figure 13 shows an example of comparison of the structures found in the FLI maps with the exact computation of the stable invariant manifolds of the Lyapunov orbit around L_3 in the case $\mu = 0.0056$, $e' = 0$, corresponding to panel A of Fig.5. The left panel shows the same structures in greater detail, plotting in red all points for which the FLI is in the limit $3.5 \leq \Psi \leq 6$. These limits exclude all points corresponding to regular orbits, as well as all escaping orbits, for which the FLI evaluation quickly saturates to a high value $\Psi \geq 50$. On the other hand, the middle panel is computed as follows. We consider the interval of Jacobi constant values $C_{min} \leq C \leq C_{max}$, where $C_{min} = 2.984$ and $C_{max} = 3.00385$ represent the minimum and maximum value of the Jacobi constant encountered in the whole 400×400 grid of initial conditions for which the FLI map of Fig.5A was computed. Splitting this interval in 400 values of C , for each value we compute numerically the corresponding horizontal Lyapunov orbit around L_3 and its stable manifold and we collect all the points in which the latter intersects the section of the FLI map (given by the pericentric condition $\lambda' - \omega - \pi/3 = 0$ as well as $x - 0.03\Delta u = 0$). Numerically, we introduce some tolerance 2×10^{-4} in the section determination, in order to collect a sufficiently large number of points necessary for visualization of the results. Plotting in the same co-ordinates as for the FLI map the collected points for all 400 stable invariant manifolds corresponding to the 400 different values of C yields the middle plot of Fig.13. The relative loss of sharpness in the picture of the manifolds is due to the numerical tolerance used in their section's determination. Despite this effect, we see clearly that the structures formed by

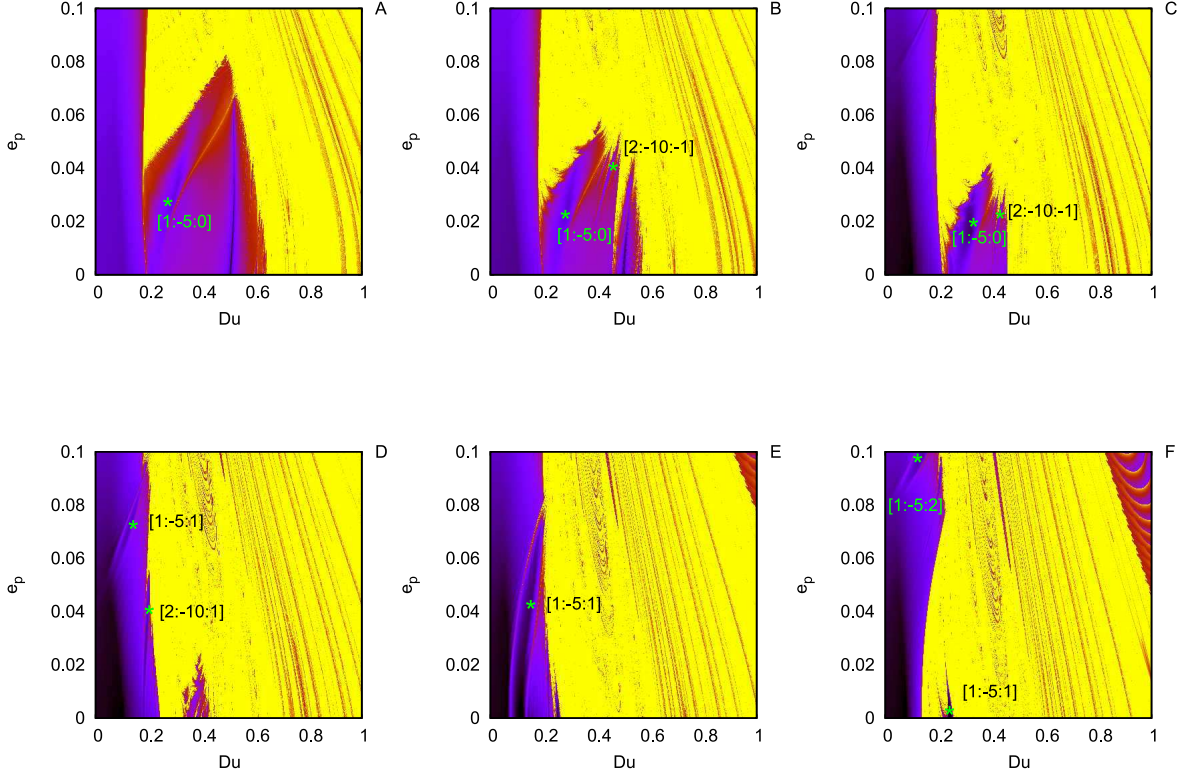


Figure 5: FLI maps for the resonance 1:5, $\mu = 0.0056$, for the values $e' = 0$ (A), $e' = 0.02$ (B), $e' = 0.04$ (C), $e' = 0.06$ (D), $e' = 0.08$ (E) and $e' = 0.1$ (F).

the invariant manifolds follow in parallel those indicated by the corresponding FLI map. The possibility to use the FLI (with a small number of iterations), in order to visualize invariant manifolds was pointed out in Guzzo and Lega (2013). Here, this effect can be considered as a manifestation of the so-called ‘Sprinkler’ algorithm (see Kovacs and Erdi 2009 for a review). Namely, in a system of fast escapes, plotting the initial conditions of the orbits which have relatively large (forward or backward) stickiness times (and, thus, relatively lower FLI values with respect to the escaping orbits) allows to visualize the (stable or unstable) manifolds of nearby periodic orbits. In fact, the sticky chaotic orbits in the forward sense of time are those trapped *within the lobes* defined by the stable invariant manifolds (see, for example, figure 19 of Efthymiopoulos et al. 1997). This effect is clearly shown in our example by combining the left and middle panels of Fig.13. Figure 13 clearly shows that the points of greater stickiness in the forward sense of time, as revealed by their relatively low (with respect to fast-escaping orbits) FLI values, are located precisely between the limits of the structures indicated by the stable invariant manifolds of the family of the planar Lyapunov orbits around L3. We note, finally that when $e' > 0$, instead of the foliation of all the manifolds of the Lyapunov family, one has to consider the invariant manifolds of a 2D unstable invariant torus around L3. This computation is numerically hardly tractable. Nevertheless, simple inspection of all panels of Fig.5 clearly shows that the structures found for $e' = 0$ essentially continue to exist, in a quite similar geometry, in the case $e' \neq 0$ as well.

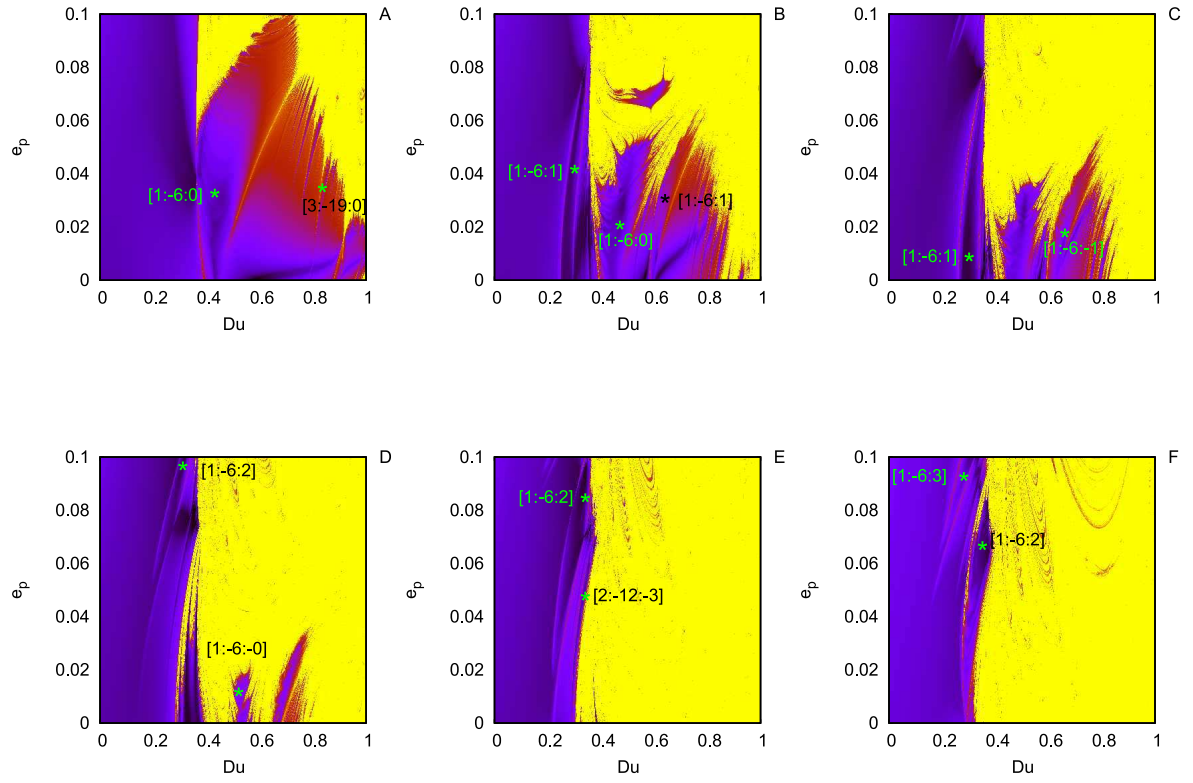


Figure 6: FLI maps for the resonance 1:6, $\mu = 0.0041$, for the values $e' = 0$ (A), $e' = 0.02$ (B), $e' = 0.04$ (C), $e' = 0.06$ (D), $e' = 0.08$ (E) and $e' = 0.1$ (F).

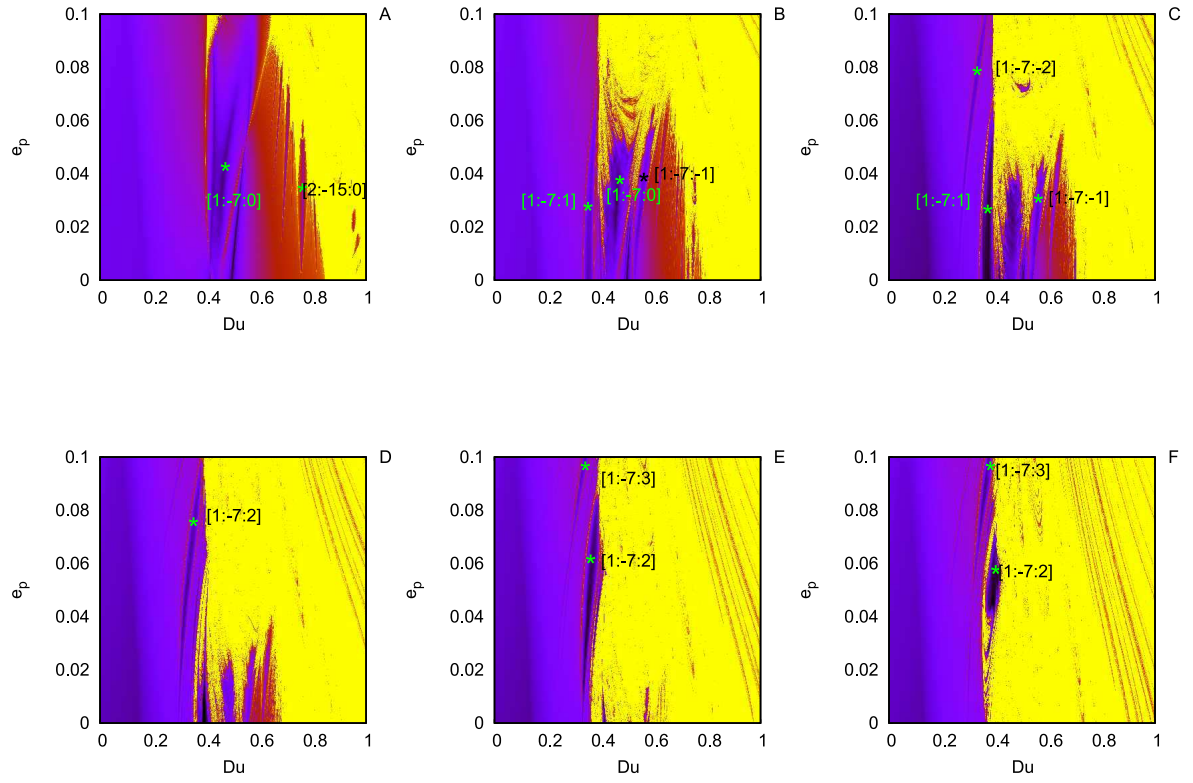


Figure 7: FLI maps for the resonance 1:7, $\mu = 0.0031$, for the values $e' = 0$ (A), $e' = 0.02$ (B), $e' = 0.04$ (C), $e' = 0.06$ (D), $e' = 0.08$ (E) and $e' = 0.1$ (F).

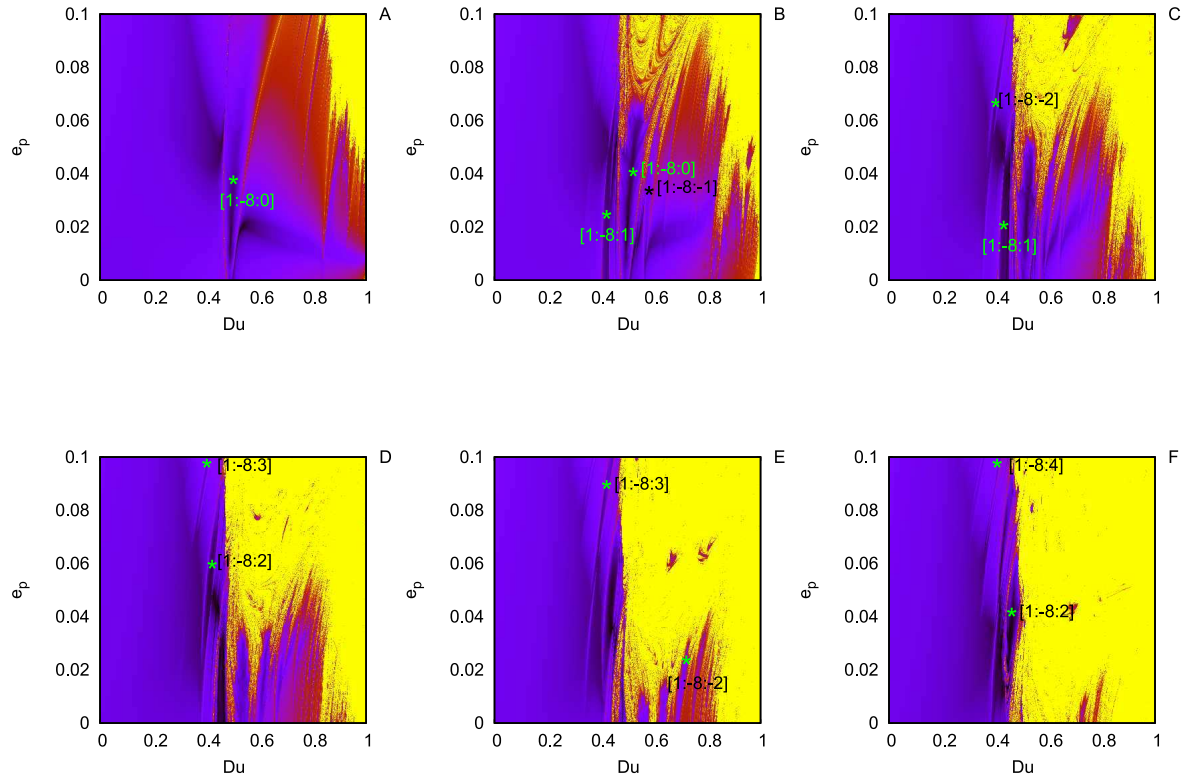


Figure 8: FLI maps for the resonance 1:8, $\mu = 0.0024$, for the values $e' = 0$ (A), $e' = 0.02$ (B), $e' = 0.04$ (C), $e' = 0.06$ (D), $e' = 0.08$ (E) and $e' = 0.1$ (F).

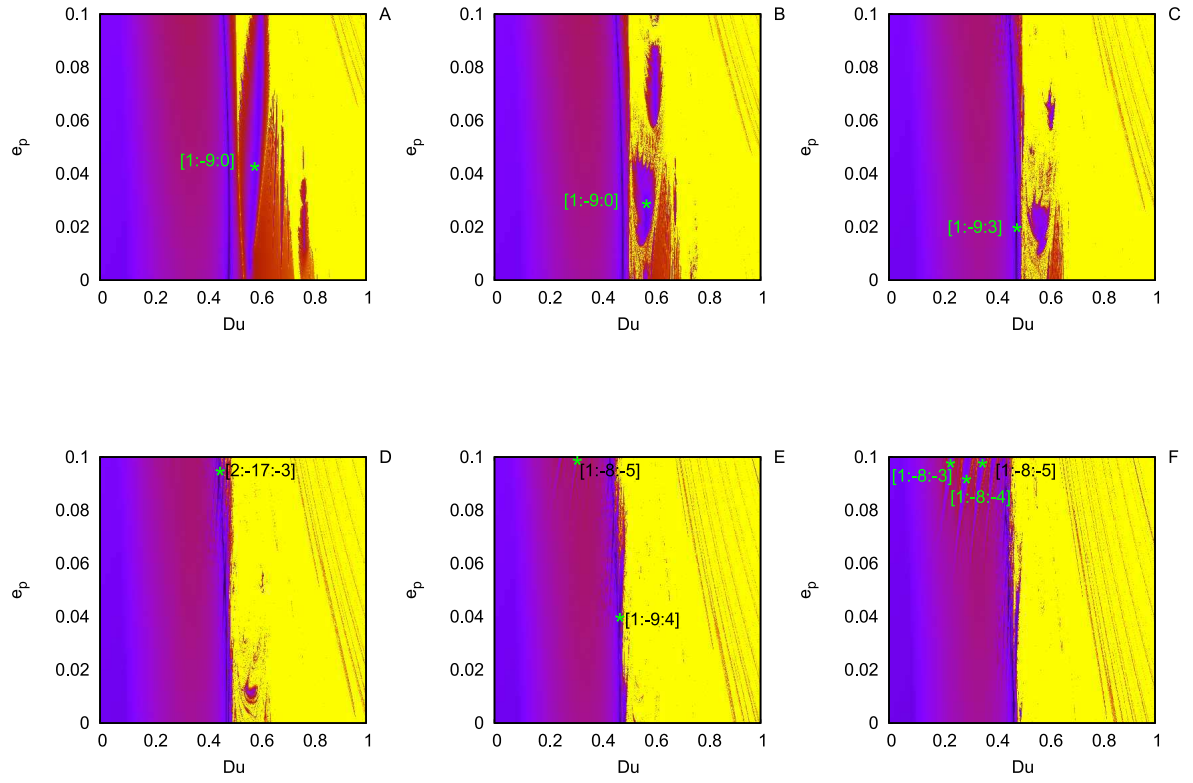


Figure 9: FLI maps for the resonance 1:9, $\mu = 0.0021$, for the values $e' = 0$ (A), $e' = 0.02$ (B), $e' = 0.04$ (C), $e' = 0.06$ (D), $e' = 0.08$ (E) and $e' = 0.1$ (F).

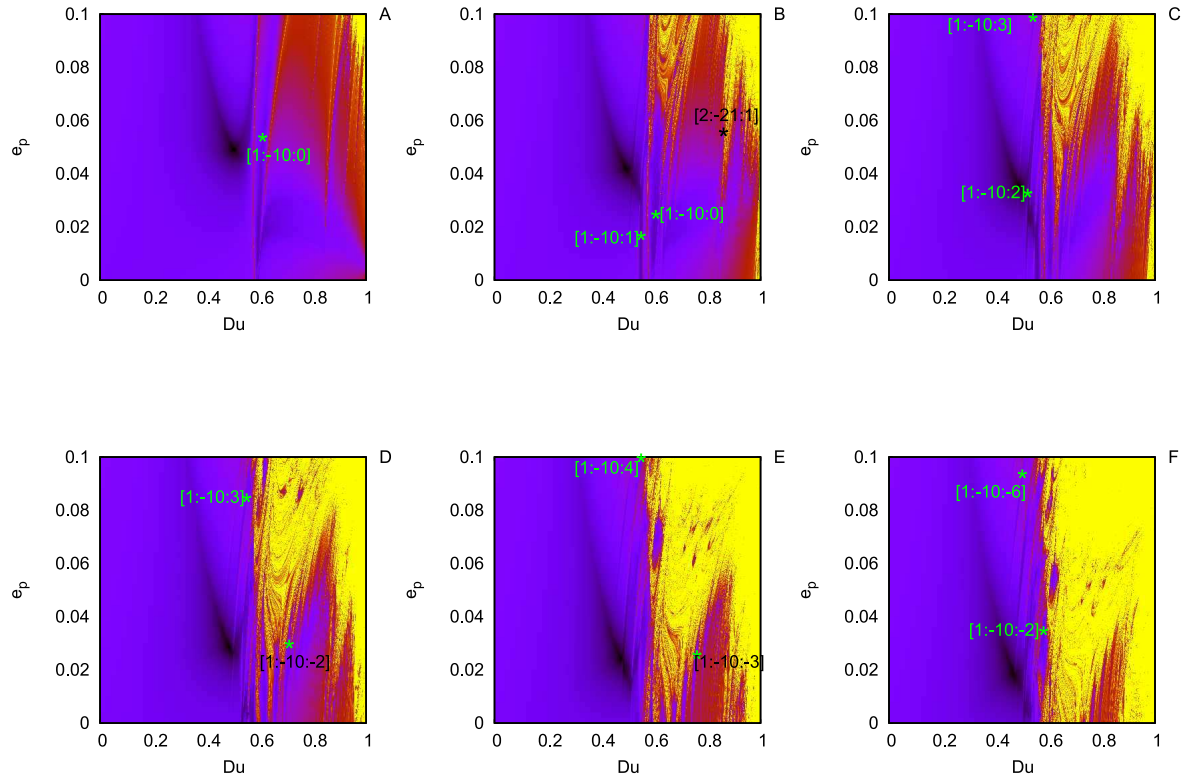


Figure 10: FLI maps for the resonance 1:10, $\mu = 0.0016$, for the values $e' = 0$ (A), $e' = 0.02$ (B), $e' = 0.04$ (C), $e' = 0.06$ (D), $e' = 0.08$ (E) and $e' = 0.1$ (F).

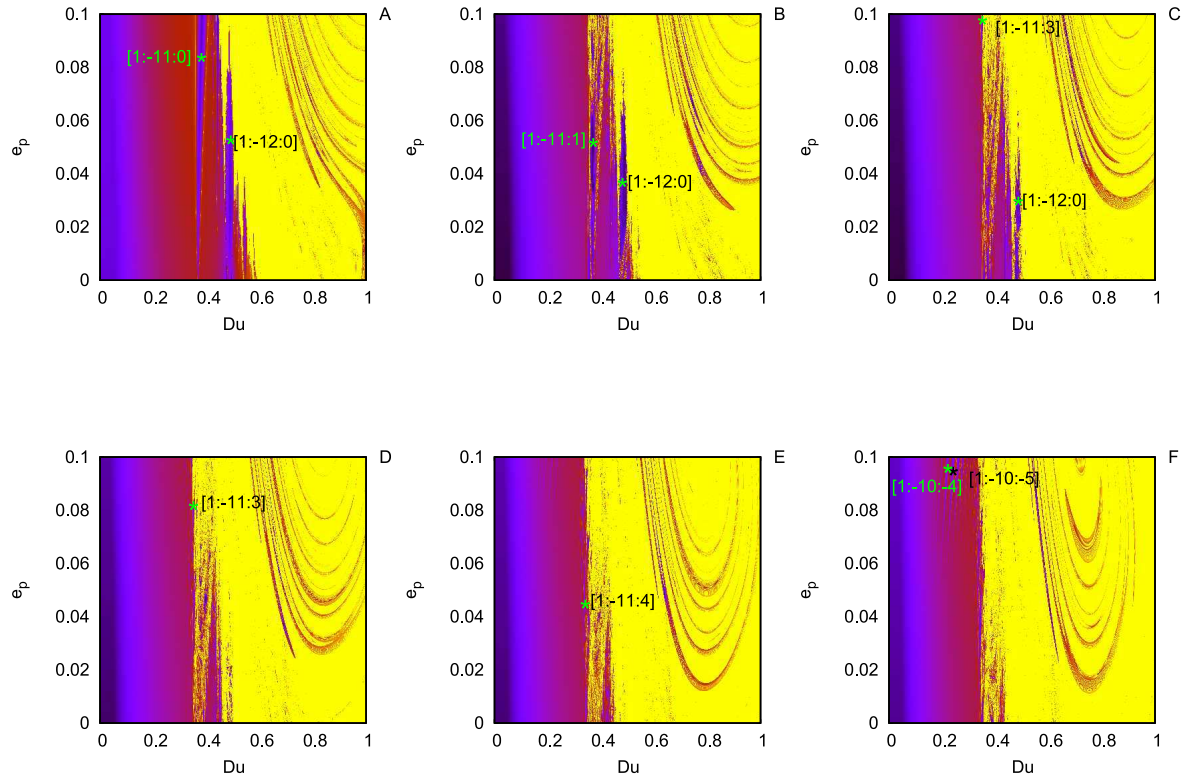


Figure 11: FLI maps for the resonance 1:11, $\mu = 0.0014$, for the values $e' = 0$ (A), $e' = 0.02$ (B), $e' = 0.04$ (C), $e' = 0.06$ (D), $e' = 0.08$ (E) and $e' = 0.1$ (F).

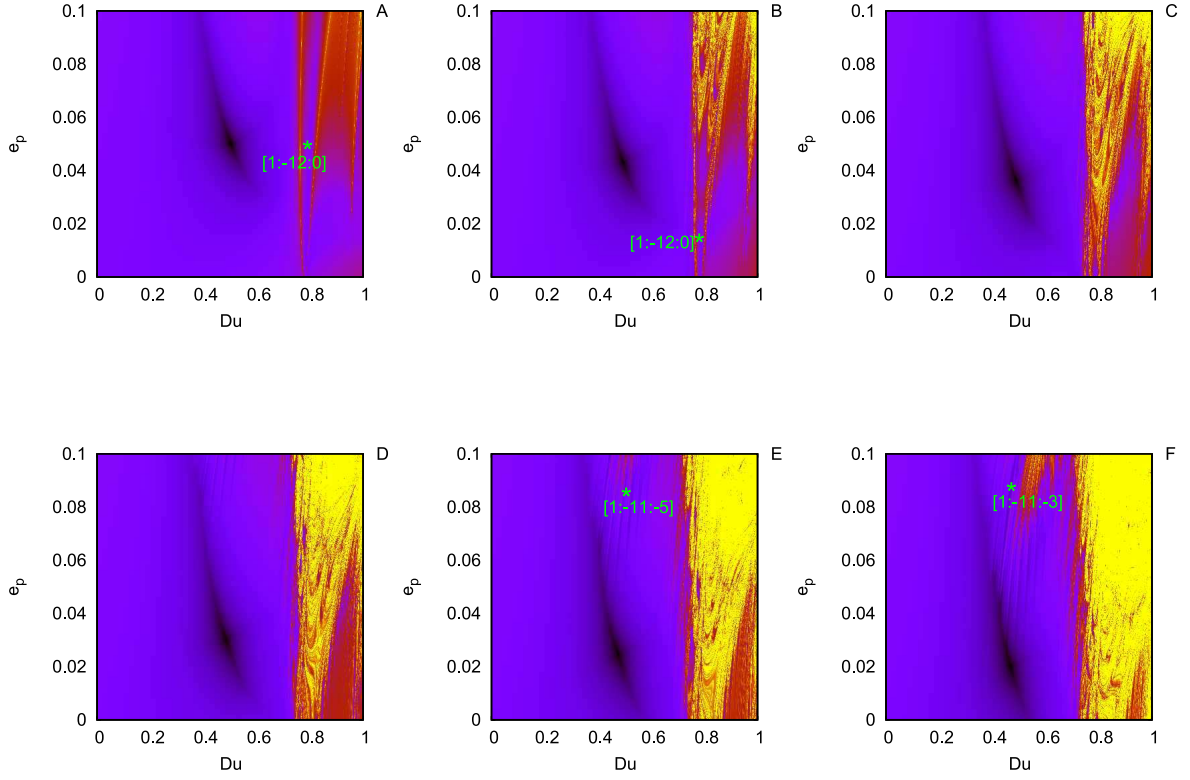


Figure 12: FLI maps for the resonance 1:12, $\mu = 0.0012$, for the values $e' = 0$ (A), $e' = 0.02$ (B), $e' = 0.04$ (C), $e' = 0.06$ (D), $e' = 0.08$ (E) and $e' = 0.1$ (F).

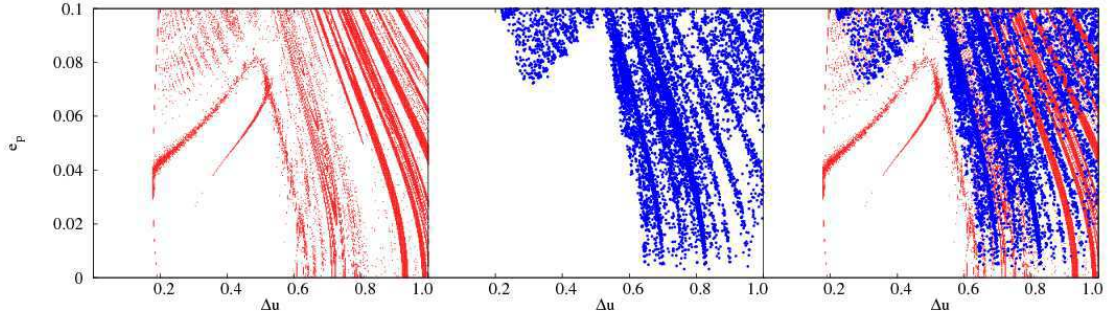


Figure 13: Left panel: All initial conditions in the 400×400 grid of Fig.5A for which the FLI value at the end of the integration is in the range $3.5 \leq \Psi \leq 6$. Middle panel: the points of intersection with the same section as for the FLI maps (see text) of the stable invariant manifolds of the family of short-period horizontal Lyapunov orbit around L3, computed for 400 different values of the Jacobi constant as indicated in the text. Right panel: superposition of the left and middle panels.

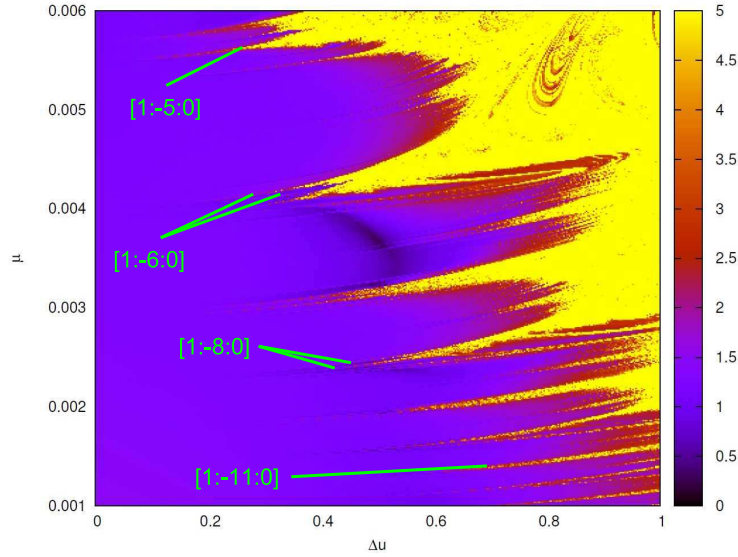


Figure 14: FLI map for a grid of 400×400 initial conditions in the plane $(\mu, \Delta u)$, for $e' = e_p = 0.02$ (see text). Dark colors (black) correspond to $\Psi = 0$ (regular orbits) and light color (yellow) to $\Psi = 5$ (chaotic orbits). The most important main resonances are labeled in the plot. Some compact bundles formed by transverse resonances near the main ones are also visible in the plot.

Returning to the discussion of the resonant structure, the overall effect of resonances on the size of the stability domain is resumed in Fig. 14. For a set of initial values of μ , from $\mu = 0.001$ to $\mu = 0.006$, with step $\Delta\mu = 1.25 \times 10^{-5}$, and fixed values for $e' = 0.02$ and $e_p = 0.02$, the figure shows the FLI map produced by integrations of the set of initial conditions given by $x = 0$, $\phi_f = -u - \frac{\pi}{3}$, $Y_f = 0$ and $\Delta u = u_0 + u$ varying from 0 to 1, with step 0.0025. Darker (black) colors correspond to regular orbits, and light (yellow) colors to chaotic orbits. The main resonances appear as long yellow tongues that contain single or double thin chaotic layers associated to the separatrix (depending on whether the resonance is odd or even). In a similar way, a large number of smaller transverse resonances fill the space between the main ones. By the fact that the tongues are nearly horizontal, we can infer that the presence of particular resonances is highly localized with respect to the value of μ , e.g. the resonance 1:6 is important at $\mu = 0.004$, it completely disappears in the chaotic domain at $\mu = 0.0045$. Also, as μ increases, a bifurcation of new secondary resonances happens less frequently. Nevertheless, since they are of decreasing order, their width and relative influence increases.

4 Chaotic diffusion

The co-existence of different types of resonances renders non-trivial the question in which domains of the phase space the chaotic diffusion, due to the interaction of resonances, provides a more efficient transport mechanism for orbits, thus affecting long term stability. As explained in section 2, two main regimes of chaotic transport exist. For isolated resonances

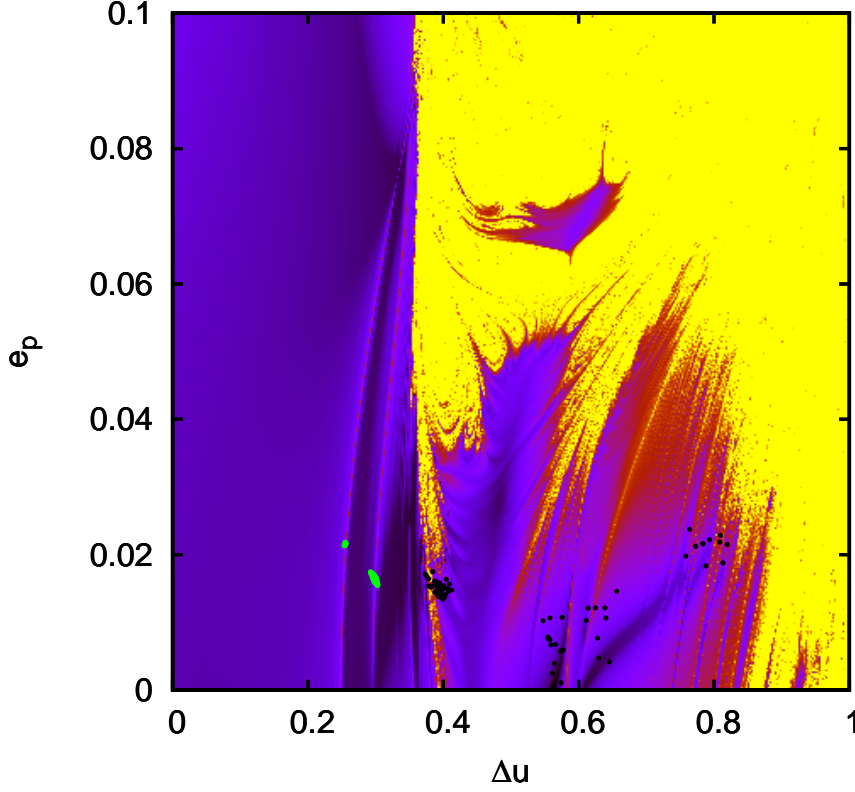


Figure 15: Different diffusion processes for two orbits with parameters $e' = 0.02$, $\mu = 0.0041$, $e_p = 0.01625$ and initial conditions $x = 0$, $\phi = \pi/3$, $Y_f = 0$ and $\Delta u = 0.299$ for the green orbit and $\Delta u = 0.376$ for the black orbit.

located inside the boundary of the main stability domain (like the transverse resonances $(1, -6, 1)$ and $(1, -6, 2)$ of Fig.4), the orbits in the stochastic layer have the possibility of slow diffusion that bears features of Arnold diffusion. In any case, we find that the diffusion rate is extremely small, thus it is practically undetectable. On the other hand, for resonances located beyond the boundary of the main stability domain, the diffusion process is best described by the paradigm of modulational diffusion. In particular, the amplitude of pulsation of the separatrix-like chaotic layers at the borders of the resonances is large enough to allow for communication of the resonances, causing the orbits to undergo abrupt *jumps* from one resonance to another, and eventually to escape.

Figure 15 provides evidence of the processes mentioned above. Two orbits are shown superposed to the FLI map for $\mu = 0.0041$, $e' = 0.02$. The initial conditions for both correspond to $e_p = 0.01625$, but different Δu ($\Delta u = 0.299$, orbit with green points, and $\Delta u = 0.376$, orbit with black points). We plot the intersection points of both orbits with the plane $(\Delta u, e_p)$ when $x = 0$, $\phi_f = 0$, with a tolerance 0.001 and 0.06 respectively. According to these data, the first orbit resides in the chaotic layer of the resonance $(1 - 6, 1)$, while the second is initially in the chaotic layer of the resonance 1:6. However, the first orbit is restricted to move essentially only along the stochastic layer of the initial resonance, as no resonance overlapping exists with any low-order adjacent resonance. As a result, the orbit's diffusion

is practically unobservable. By contrast, the second orbit suffers a significant change of topology over a timescale of only 10^5 periods. The orbit visits many other resonances besides the starting one, jumping stochastically between the chaotic layers of the resonances 1:6. $(1, -6, -1)$, $(1, -6, -2)$, $(3, -19, 2)$, and $(3, -19, 1)$, and possibly other ones of higher order. The proper eccentricity e_p also exhibits abrupt jumps in the interval $[0.001, 0.025]$.

The long-term behavior of orbits in the modulational diffusion regime can be characterized by a statistical study. To this end, we consider an ensemble of orbits in a rectangle of initial conditions. As an example, setting, as before, $\mu = 0.0041$, $e' = 0.02$, we consider a 60×60 grid of initial conditions in the interval $0.33 \leq \Delta u \leq 0.93$, $0 \leq e_p \leq 0.06$, with the remaining initial conditions defined as for the FLI maps above. The ensembles were processed at 5 different snapshots, corresponding to the integration times of $T = 10^3, 10^4, 10^5, 10^6$ and 10^7 periods. In every snapshot (of final time T), the orbits are classified in three distinct groups:

Regular orbits: these are orbits whose value of the FLI satisfies the condition

$$\Psi(T) < \log_{10}\left(\frac{N}{10}\right) \quad (38)$$

where N is the total number of periods for the integration. Since for regular orbits the FLI grows linearly with N , the threshold of Eq.(38) allows to identify orbits which can be clearly characterized as regular. These orbits are exempt from further integration.

Escaping orbits: an orbit is considered as escaping if the orbit undergoes a sudden jump in the numerical energy error ΔH greater than 10^{-3} . This threshold is determined by the requirement that the jump surpasses by about two orders of magnitude the worst possible accumulation of round-off energy errors at the end of the integration time (i.e. after 10^7 periods). We tested the cumulative energy error as a function of time for different initial conditions. Figure 16 shows the evolution of ΔH for one example of escaping orbit. The first panel shows the increment of ΔH up to a time $t = 4600$. The absolute cumulative error grows linearly in time at a rate $\sim 4 \times 10^{-13}$ per period. This rate is characteristic of the orbits in the thin chaotic layers between the resonances. However, ΔH exhibits an abrupt variation $\Delta H = 4 \times 10^{-3}$ at the moment of escape. Up to the maximum integration time 10^7 , the cumulative energy error for non-escaping orbits is smaller than 4×10^{-6} . Thus, we set a safe threshold value for escape identifications as $\Delta H_{esc} = 10^{-3}$.

Transition orbits: we characterize as transition orbits those whose FLI value violates condition (38), but which do not escape during the integration up to the time T . As we will see, part of these orbits remain at low FLI values up to the end of the integration, yielding a growth $\Psi \sim \log(T)$. Thus, the orbits exhibit a regular behavior up to at least 10^7 periods. However, a second sub-group is formed among the transition orbits, containing truly sticky orbits with positive Lyapunov exponents and FLI values growing asymptotically linearly with T .

With the results at the five different snapshots, a statistical study of the escaping times is constructed as follows: in the end of every snapshot, i) we count the number of orbits belonging to each of the three groups, ii) we compute the histogram of FLI values (from 0

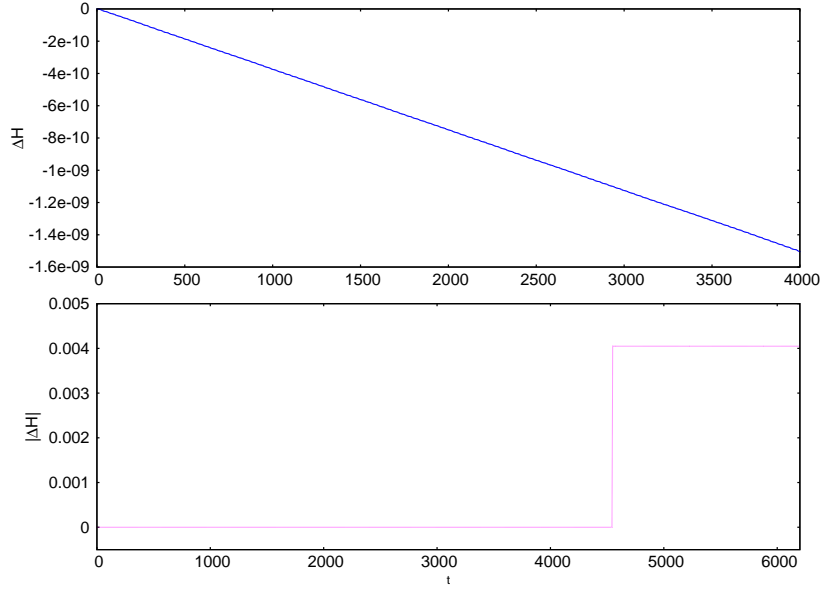


Figure 16: Time evolution of the value of the round-off cumulative energy error ΔH of an orbit that escapes at $t \sim 4600$.

up to 50) for the transition orbits, and iii) we store the values of ΔH and Ψ for both the escaping and the transition orbits. The results of (i) are summarized in the following table:

Snapshot	(N. of periods)	Regular	Transition	Escaping
1	10^3	1220 (33.8%)	2027 (56.3%)	353 (9.9%)
2	10^4	1263 (35%)	1388 (38.5%)	949 (26.5%)
3	10^5	1296 (36%)	966 (26.8%)	1338 (37.2%)
4	10^6	1299 (36.1%)	699 (19.4%)	1602 (44.5%)
5	10^7	1309 (36.3%)	603 (16.8%)	1688 (46.9%)

Focusing, now, on the groups of transition and escaping orbits, the upper panels in Fig. 17a-e show the distribution of ΔH and FLI (Ψ) values for the transition orbits (blue) and the escaping orbits (red) respectively. In Fig.17a (upper panel), for $T = 10^3$ periods, most of the transition orbits are found to keep a relatively low value of the FLI, $\Psi < 10$, and a cumulative energy error ΔH of about 10^{-9} . In fact, *all* the transition orbits with larger ΔH become escaping orbits shortly after $T = 10^3$ periods. A second group of transition orbits, however, starts being formed, with FLI larger than or equal to 50. The lower panel shows the distribution of FLI values for all the transition orbits. The left concentration represents regular or very sticky orbits, while the more chaotic orbits are spread over larger values of the FLI, with a small secondary peak formed in the right part of the histogram at $\Psi = 50$. However, as the integration time increases, a ‘stream’ is formed that transports members of the left group towards the right group. As a result, at the last snapshot, ($T = 10^7$ periods), the right group contains about 30% of the transition orbits and 6% of the total orbits considered. In fact, as visually clear in all upper panels of Fig.17, most escapes occur at intermediate

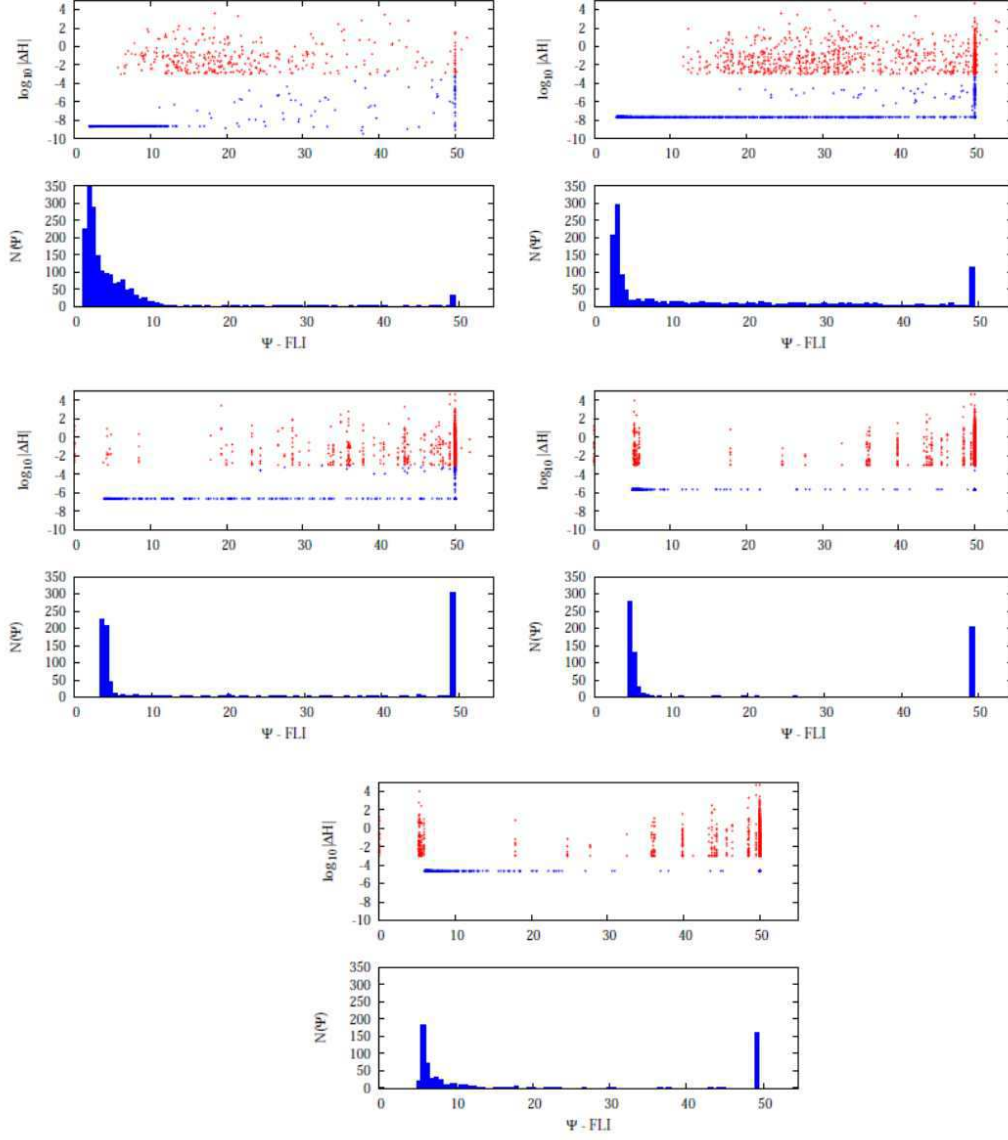


Figure 17: Cumulative energy round-off error ΔH vs FLI value for the groups of transitions (blue) and escaping (red) orbits, as well as the distribution of the FLI values for the transition group. The different panels refer to the time snapshots $T = 10^3$ (a), $T = 10^4$ (b), $T = 10^5$ (c), $T = 10^6$ (d) and $T = 10^7$ (e) periods of the primaries.

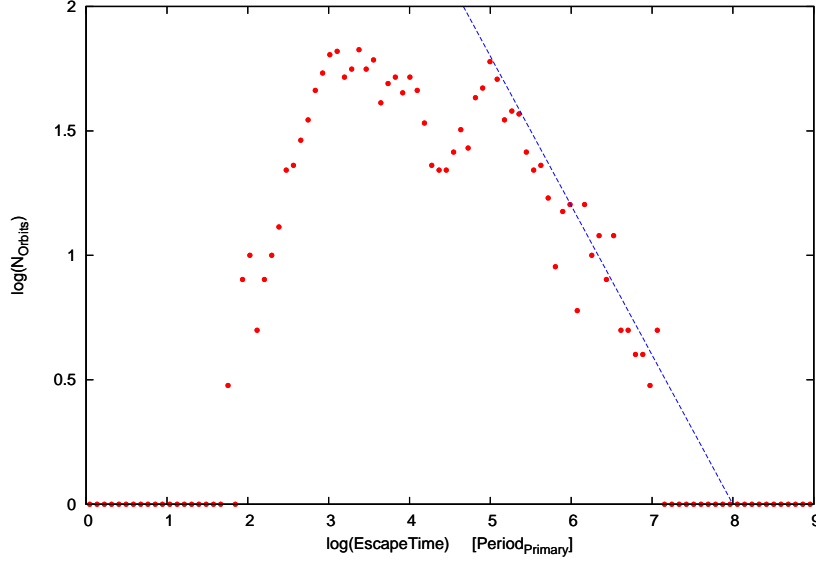


Figure 18: Histogram of escaping times for the escaping orbits.

values of the FLI, while the right group is nearly completely detached from the left group of the transition orbits, the latter moving to the right at a speed logarithmic in T , i.e. as expected for regular orbits. Finally, the Lyapunov characteristic times of the orbits in the right group are all substantially smaller than $T_L = 10^5$, while the orbits remain sticky for times $T_{stickiness} > 2\pi 10^7$. This behaviour is reminiscent of *stable chaos*.

Finally, we notice that the escaping orbits (red) seem to form bands of preferential values of the FLI. We have not fully identified the origin of these bands. Nevertheless, they could be connected to the fact that the escape can occur only via the thin chaotic layers between the resonances, so that the concentration to particular FLI values could reflect the local FLI value for orbits residing for long time within each one of such layers.

Figure 18 shows the histogram of escaping times of all the escaping orbits. It becomes evident that in the process of escaping two distinct timescales can be distinguished, corresponding to two peaks of the histogram. The first peak, at about 10^3 periods, corresponds to fast escapes, while the second, at about 10^5 periods, corresponds to slow escapes. As shown below, the large majority of fast escaping orbits are with initial conditions within the chaotic sea surrounding the resonances, while slowly escaping orbits are those with initial conditions in the thin chaotic layers delimiting the resonances. In the latter case, we find that beyond a time $t \approx 10^5$ periods, the distribution of the escape times shows a *power-law* tail. The straight line in Fig.18 represents a power-law fit

$$P(t_{esc}) \propto t_{esc}^{-\alpha}, \quad \alpha \approx 0.8 \quad . \quad (39)$$

We note in this respect that power-law statistics of the escape times are a characteristic feature of stickiness and long-term chaotic correlations of chaotic orbits (see Meiss 1992, p. 843 and references therein, and also Ding et al 1990, Cheng et al 1992).

Finally, Fig.19 shows a comparison between FLI values and the residence (or escape) times for all the orbits of the integrated ensemble. The left panel shows the FLI map for

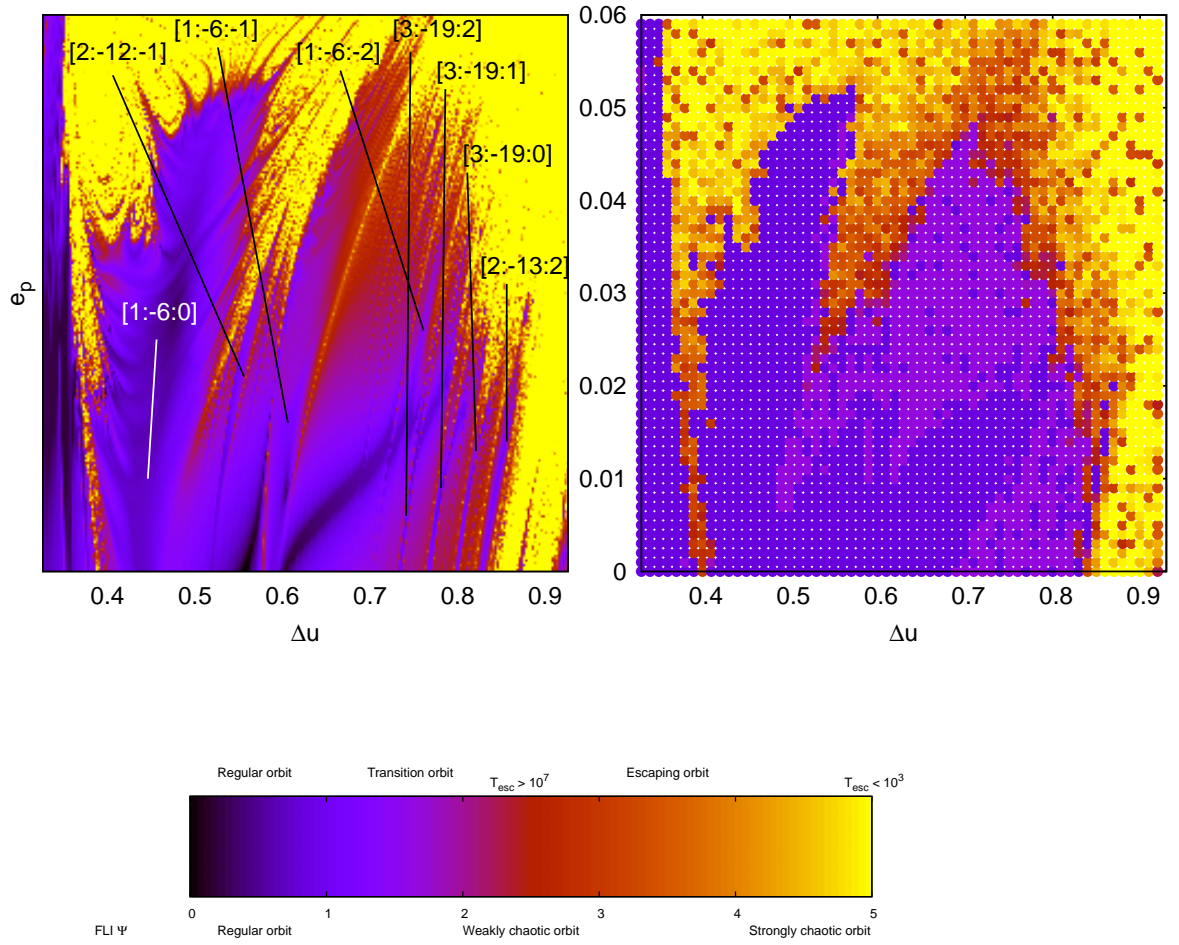


Figure 19: FLI map for the grid of initial conditions $[0.33, 0.93] \times [0.00, 0.06]$ in the plane $(\Delta u, e_p)$ (left panel) and color map of the escaping times for the same grid (right panel), in both cases with parameters $\mu = 0.0041$ and $e' = 0.02$. See text for more details.

the square of initial conditions $[0.33, 0.93] \times [0.00, 0.06]$. The right panel, now, shows in color scale the residence, or escaping times, for all 3600 initial conditions of the ensemble. Yellow colors represent the faster escaping times ($t_{esc} < 10^3$ periods), while red the slower (between 10^6 and 10^7 periods). In light purple are depicted the orbits that remain in the group of transition orbits up to the end of the integration (10^7 periods), while deep purple represents the orbits belonging to the regular group. The first observation is that the distribution of escaping times reproduces to some extent the main features of the resonant structure found by the stability map. In particular, the chaotic layer of the resonance 1:6 appears clearly marked by long escape times (larger than 10^5 periods). The stickiness is in general enhanced at the borders of all resonances. On the other hand, most of the orbits with $\Psi = 5$ or greater, that are qualified as chaotic in the stability map, belong to the population of fast escapes, and we find that most need less than 10^3 periods to escape. But the most interesting feature is that all the thin chaotic layers around the resonances $(2, -12, -1)$, $(1, -6, -1)$, $(1, -6, -2)$, $(3, -19, 2)$, $(3, -19, 1)$, $(3, -19, -0)$, and $(2, -13, 2)$, contain orbits that appear *not escaping* at least up to 10^7 periods. This, despite the fact that some of these orbits are relatively strongly chaotic, i.e with Ψ close to 5. Thus, we can conclude that the stickiness phenomena in the thin chaotic layers formed in the resonant domains of the action space can prolong the stability of hypothetical trojan planets up to times comparable to the age of the hosting system. Consequently, the resonant domains beyond the main stability domain are also candidates to host trojan companions of giant extrasolar planets.

5 Conclusions

In this work, we present a parametric study of the resonant structure in the co-orbital domain, as well as the main types and associated timescales for chaotic diffusion of hypothetical small (considered massless) trojan companions of giant planets in extrasolar planetary systems.

First, we introduce a Hamiltonian formalism in terms of modified Delaunay action-angle variables, allowing to take various secular effects into account. In particular, while we presently deal in detail with the planar ERTBP, the proposed formalism allows for generalizations in the case of more than one planet, as well as non-zero inclinations of the exoplanets. This formulation permits us to define a hierarchy of Hamiltonian models corresponding to different levels of perturbation on the trojan planetary motion. In particular, the hamiltonian H_b (eq. (18)) represents a system of two degrees of freedom that describes the synodic (guiding-center) and short period motions of the trojan planet. Its associated parameters J_s , Y_p serve as constants of motion (proper elements). Furthermore, modulo a redefinition of variables, the form of H_b is identical in the ERTBP and in the RMPP. The full hamiltonian consists of H_b + terms describing the secular effects due to the primary or to additional perturbing planets. We classified resonances between the short-period, synodic and secular frequencies, in three types: *main*, *transverse* and *secular*.

On the other hand, by means of numerical experiments in the planar ERTBP, we depict the form of the corresponding web of resonances in the space of proper elements. With a parametric study for various values of μ (in the range $0.001 \leq \mu \leq 0.006$) and e' ($e' \leq 0.1$) for the giant primary, we produce phase portraits and stability maps.

In the phase portraits, we found that the resonant orbits move outwards as the proper eccentricity $e_p = \sqrt{-2Y_p}$ increases, and the corresponding stability islands grow. For small

values of e_p the stability islands are surrounded by invariant tori. Small higher order resonances are present at the border of the stability domain. Since as e_p increases the resonant islands grow in size, most of their surrounding invariant tori are destroyed. For a critical value of e_p , the last KAM torus surrounding the resonant island chain is destroyed, and the chaotic sea penetrate deeper inside the main stability domain.

Similar phenomena occur by varying the mass parameter μ . In this case, different values of μ give rise to different resonances. Thus, the size of the domain of stability suffers abrupt variations connected to the bifurcations of new resonances. On the other hand, the size of the non-resonant domain does not change much with variations on e' . However, the resonant domain, which for low values of e' is full of transverse resonances, quickly shrinks within the chaotic region, and for values of e' beyond 0.1, it completely disappears.

We also present some main types of chaotic diffusion observed by the integrations of orbits with initial conditions in the resonance web. We found two different kinds of diffusion processes, depending on the width of the pulsation of the separatrices. For resonances with small pulsation widths, or isolated (as the transverse resonances that penetrate the domain of stability), the separatrices of one resonance do not enter to the pulsation domain of nearby resonances. Then, the rate of the chaotic diffusion is practically undetectable. On the other hand, for resonances with large pulsation widths, or closely spaced multiplets, the separatrices of more than one nearby resonances overlap, and the process of diffusion accelerates, with timescale of the order of 1Myr. This type of diffusion is best described by models of modulational diffusion.

Integrating ensembles of orbits, we produce a statistical study of the escape probabilities as a function of the escape time. Two distinct escaping timescales are identified (fast and slow), characterized by two peaks in the corresponding histogram. The slow escapes exhibit a power-law distribution of the escaping times, which is characteristic of stickiness and long-term correlations of weakly chaotic orbits.

Finally, we compare the results of the escaping (or residence) times, with the results produced by the FLI maps for the same parameter and set of initial conditions. We conclude that: i) the distribution of escaping times reproduces to some extent the resonant structure found by the FLI map. ii) Sticky orbits are located at the borders of the resonant domain. Besides, the orbits qualified as chaotic in the stability map, show fast escapes and need less than 10^3 periods for escaping. Finally, iii) the thin chaotic layers in the resonant domain contain orbits that appear not escaping at least up to 10^7 periods, despite the fact that most of these orbits are quite strongly chaotic. As a result, the stickiness phenomena of these thin chaotic layers can prolong the stability of hypothetical trojan planets up to the lifetime of their hosting system.

Acknowledgements: The authors would like to thank Professors Z. Knezevic and U. Locatelli for their useful remarks, and the anonymous referees for helping to improve the original manuscript. R.I.P. is supported by the Astronet-II Marie Curie Training Network (PITN-GA-2011-289240). C.E. acknowledges support by the Grant 200/815 of the Research Committee of the Academy of Athens.

References

- [1] Arnold, V. I.: Instability of dynamical systems with several degrees of freedom, *Sov. Math. Dokt.* **5**, 581-585 (1964)
- [2] Beaugé, C., and Roig, F.: A semianalytical model for the motion of the Trojan asteroids: proper elements and families, *Icarus* **153**, 391-415 (2001)
- [3] Beaugé, C., Sándor, Z., Érdi, B., and Süli, A.: Co-orbital terrestrial planets in exoplanetary systems: a formation scenario, *Astron. Astrophys.* **463**, 359-367 (2007)
- [4] Bien, R., and Schubart, J.: Three characteristic orbital parameters for the Trojan group of asteroids, *Astron. Astrophys.* **175**, 292-298 (1987)
- [5] Brown, E. W., Shook, C. A.: *Planetary Theory*. New York, Cambridge University Press, p. 256 (1964)
- [6] Celletti, A., Giorgilli, A.: On the stability of the Lagrangian points in the spatial restricted problem of three bodies, *Celest. Mech. Dyn. Astron.* **50**, 31-58 (1991)
- [7] Chirikov, B. V., Lieberman, M. A., Shepelyansky, D. L., and Vivaldi, F. M.: A theory of modulational diffusion, *Physica D* **14**, 289-304 (1985)
- [8] Cresswell, P., and Nelson, R. P.: On the growth and stability of Trojan planets, *Astron. Astrophys.* **493**, 1141-1147 (2009)
- [9] Deprit, A.: Limiting orbits around the equilateral centers of libration, *Astron. J.* **71**, 77-87 (1966)
- [10] Deprit, A., and Rabe, E.: Periodic trojan orbits for the resonances 1/12, *Astron. J.* **74**, 317-320 (1968)
- [11] Deprit, A., and Price, J.F.: L'espace de phase autour de L_4 pour la résonance interne 1/3, *Astron. Astrophys.* **1**, 427-430 (1969)
- [12] Deprit, A., and Henrard, J.: Sur les orbites périodiques issues de L_4 à la résonance interne 1/4, *Astron. Astrophys.* **3**, 88-93 (1969)
- [13] Ding, M., Bountis, T., and Ott, E.: Algebraic escape in higher dimensional Hamiltonian systems, *Phys. Lett. A* **151**, 395-400 (1990)
- [14] Dobrovolskis, A.: Effects of Trojan exoplanets on the reflex motions of their parent stars, *Icarus* **226**, 1636-1641 (2013)
- [15] Dullin, H. R., and Worthington, J. I.: The vanishing twist in the restricted three body problem, *arXiv:1309.1280 [math-ph]* (2013)
- [16] Dvorak, R., Pilat-Lohinger, E., Schwarz, R., and Freistetter, F.: Extrasolar Trojan planets close to habitable zones, *Astron. Astrophys.* **426**, 37-40 (2004)
- [17] Efthymiopoulos C., Contopoulos G., Voglis, N., and Dvorak, R.: Stickiness and Cantori, *J. Phys. A Math. Gen.* **30**, 8167-8186 (1997)

- [18] Efthymiopoulos, C., Sándor Z.: Optimized Nekhoroshev estimates for the Trojan asteroids with a symplectic mapping model of co-orbital motion, *MNRAS* **364**, 253-271 (2005)
- [19] Efthymiopoulos, C.: High order normal form stability estimates for co-orbital motion, *Celest. Mech. Dyn. Astron.* **117**, 101-112 (2013)
- [20] Efthymiopoulos, C., and Páez, R. I.: *in preparation* (2014)
- [21] Érdi, B.: Long periodic perturbations of Trojan asteroids, *Celest. Mech. Dyn. Astron.* **43**, 303-308 (1988)
- [22] Érdi, B.: The Trojan problem, *Celest. Mech. Dyn. Astron.* **65**, 149-164 (1997)
- [23] Erdi B., Sándor Zs.: Stability of co-orbital motion in exoplanetary systems, *Celest. Mech. Dyn. Astron.* **92**, 113-121 (2005)
- [24] Érdi B., Nagy I, Sándor Zs., Süli, A., Fröhlich G.: Secondary resonances of co-orbital motions, *MNRAS* **381**, 33-40 (2007)
- [25] Érdi, B., Forgács-Dajka, E., Nagy, I., Rajnai, R.: A parametric study of stability and resonances around L_4 in the elliptic restricted three-body problem, *Celest. Mech. Dyn. Astron.* **104**, 145-158 (2009)
- [26] Froeschlé, C., Guzzo, M., Lega, E.: Graphical evolution of the Arnold web: from order to chaos, *Science* **289**, 2108-2110 (2000)
- [27] Funk, B., Schwarz., R., Süli, A., and Érdi, B.: On the stability of possible Trojan planets in the habitable zone: an application to the systems HB 147513 and HD 210277, *MNRAS* **423**, 3074-2082 (2012)
- [28] Gabern, F., Jorba, A., and Locatelli, U.: On the construction of the Kolmogorov normal form for the Trojan asteroids, *Nonlinearity* **18**, 1705-1734 (2005)
- [29] Garfinkel, B.: Theory of the Trojan asteroids, Part I, *Astron. J.* **85**, 368-379 (1977)
- [30] Giorgilli, A., and Skokos, Ch.: On the stability of the Trojan asteroids, *Astron. Astrophys* **317**, 254-261 (1997)
- [31] Giuppone, C. A., Benítez-Llambay, P., and Beaugé, C.: Origin and detectability of coorbital planets from radial velocity data, *MNRAS* **421**, 356-368 (2012)
- [32] Guzzo, M., and Lega, E.: Evolution of the tangent vectors and localization of the stable and unstable manifolds of hyperbolic orbits by Fast Lyapunov Indicators, *ArXiv* 1307.6731 (2013)
- [33] Haghighipour, N., Capen, S., Hinse, T.: Detection of Earth-mass and super-Earth Trojan planets using transit timing variation method, *Cel. Mech. Dyn. Astron.* **117**, 75-89 (2013)
- [34] Kovács, T., and Erdi, B.: Transient chaos in the Sitnikov problem, *Cel. Mech. Dyn. Astron.* **105**, 289-304 (2009)

- [35] Lai, Y. C., Ding, M., Grebogi, C., Blümel, R.: Algebraic decay and fluctuations of the decay exponent in Hamiltonian systems, *Phys. Rec. A* **46**, 4661-4669 (1992)
- [36] Laskar, J.: The chaotic motion of the solar system: A numerical estimate for the size of the chaotic zones, *Icarus* **88**, 266-291 (1990)
- [37] Laskar, J., Joutel, F., and Boudin, F.: Orbital, precessional, and insolation quantities for the Earth from -20Myr to $+10\text{Myr}$, *Astron. Astrophys.* **270**, 522-533 (1993)
- [38] Laughlin, G., and Chambers, J.: Extrasolar Trojans: the viability and detectability of planets in the 1:1 resonance, *Astroph. J.* **124**, 592-600 (2002)
- [39] Levison, H., Shoemaker, E. M., Shoemaker, C. S.: Dynamical evolution of Jupiter's Trojan asteroids, *Nature* **385**, 42-44 (1997)
- [40] Libert, A.S., and Sansottera, M.: On the extension of the Laplace-Lagrange secular theory to order two in the masses for extrasolar systems, *Cel. Mech. Dyn. Astron.* **117**, 149-168 (2013)
- [41] Lohinger, E., and Dvorak, R.: Stability regions around L_4 in the elliptic restricted problem, *Astron. Astrophys.* **280**, 683-687 (1993)
- [42] Lhotka, Ch., Efthymiopoulos C., and Dvorak, R.: Nekhoroshev stability at L_4 or L_5 in the elliptic-restricted three-body problem - application to Trojan asteroids, *MNRAS* **384**, 1165-1177 (2008)
- [43] Lyra, W., Johansen, A., Klahr, H., and Piskunov, N.: Standing on the shoulders of giants. Trojan Earths and vortex trapping in low mass self-gravitating protoplanetary disks of gas and solids, *Astron. Astrophys.* **493**, 1125-1139 (2009)
- [44] Marzari, F., Tricarino P., and Scholl, H.: Stability of Jupiter Trojans investigated using frequency map analysis: the MATROS project, *MNRAS* **345**, 1091-1100 (2003)
- [45] Meiss, J. D.: Symplectic maps, variation principles and transport, *Rev. Mod. Phys.* **64**, 795-848 (1992)
- [46] Menou, K., and Tabachnik, S.: Dynamical habitability of known extrasolar planetary systems, *Astroph. J.* **583**, 473-488 (2003)
- [47] Milani A.: The Trojan asteroid belt: Proper elements, stability, chaos and families, *Celest. Mech. Dyn. Astron.* **57**, 59-94 (1993)
- [48] Morbidelli, A.: *Modern Celestial Mechanics. Aspects of Solar System Dynamics*, Taylor and Francis, London (2002)
- [49] Morais, M. H. M.: Hamiltonian formulation of the secular theory for Trojan-type motion, *Astron. Astrophys.* **369**, 677-689 (2001)
- [50] Murray, C.D., Dermott, S.F.: *Solar System Dynamics*, Cambridge University Press. (1999)

- [51] Namouni, F., and Murray, C.D.: The effect of eccentricity and inclination on the motion near the lagrangian points L_4 and L_5 , *Celest. Mech. Dyn. Astron.* **76**, 131-138 (2000)
- [52] Rabe, E.: Third-order stability of the Long-period Trojan librations, *Astron. J.* **72**, 10-17 (1967)
- [53] Robutel, P., Gabern, F., Jorba, A.: The observed Trojans and the global dynamics around the lagrangian points of the Sun-Jupiter system, *Celest. Mech. Dyn. Astron.* **92**, 53-69 (2005)
- [54] Robutel, P., Gabern, F.: The resonant structure of Jupiter's Trojan asteroids - I. Long-term stability and diffusion, *MNRAS* **372**, 1463-1482 (2006)
- [55] Robutel, P., Bodossian, J.: The resonant structure of Jupiter's Trojan asteroids - II. What happens for different configurations of the planetary systems, *MNRAS* **399**, 69-87 (2009)
- [56] Schwarz, R., Dvorak, R., Süli, A, and Érdi B.: Survey of the stability region of hypothetical habitable Trojan planets, *Astron. Astrophys.* **474**, 1023-11029 (2007)
- [57] Tsiganis, K., Varvoglis, H., Dvorak, R.: Chaotic diffusion and effective detectability of Jupiter Trojans, *Celest. Mech. Dyn. Astron.* **92**, 71-87 (2005)

6 Appendix

6.1 Averaged Hamiltonian $\langle H \rangle$

Up to the second order in e and e'_0 , and first order in μ , the averaged Hamiltonian $\langle H \rangle$ of Eq.(12) is given by

$$\begin{aligned}
\langle H \rangle = & -\frac{1}{2(1+x)^2} - x + J_3 - g' y + \frac{\mu}{a} + a e e'_0 \mu \cos(\beta - 2\tau) + a \mu \cos(\tau) \\
& - \frac{1}{2} a e^2 \mu \cos(\tau) - \frac{1}{2} a e_0'^2 \mu \cos(\tau) - \frac{15 a^2 e^2 \mu}{8(1+a^2-2a\cos(\tau))^{5/2}} - \frac{3 a^4 e^2 \mu}{4(1+a^2-2a\cos(\tau))^{5/2}} \\
& - \frac{3 e_0'^2 \mu}{4(1+a^2-2a\cos(\tau))^{5/2}} - \frac{15 a^2 e_0'^2 \mu}{8(1+a^2-2a\cos(\tau))^{5/2}} + \frac{9 a e e'_0 \mu \cos(\beta)}{4(1+a^2-2a\cos(\tau))^{5/2}} \\
& + \frac{9 a^3 e e'_0 \mu \cos(\beta)}{4(1+a^2-2a\cos(\tau))^{5/2}} - \frac{3 a^2 e e'_0 \mu \cos(\beta - 3\tau)}{8(1+a^2-2a\cos(\tau))^{5/2}} - \frac{3 a e e'_0 \mu \cos(\beta - 2\tau)}{4(1+a^2-2a\cos(\tau))^{5/2}} \\
& - \frac{3 a^3 e e'_0 \mu \cos(\beta - 2\tau)}{4(1+a^2-2a\cos(\tau))^{5/2}} + \frac{3 a^2 e e'_0 \mu \cos(\beta - \tau)}{4(1+a^2-2a\cos(\tau))^{5/2}} + \frac{3 a^3 e^2 \mu \cos(\tau)}{2(1+a^2-2a\cos(\tau))^{5/2}} \\
& + \frac{3 a e_0'^2 \mu \cos(\tau)}{2(1+a^2-2a\cos(\tau))^{5/2}} + \frac{3 a^2 e^2 \mu}{4(1+a^2-2a\cos(\tau))^{3/2}} + \frac{3 e_0'^2 \mu}{4(1+a^2-2a\cos(\tau))^{3/2}} \\
& - \frac{9 a e e'_0 \mu \cos(\beta)}{4(1+a^2-2a\cos(\tau))^{3/2}} - \frac{a e e'_0 \mu \cos(\beta - 2\tau)}{4(1+a^2-2a\cos(\tau))^{3/2}} + \frac{a e^2 \mu \cos(\tau)}{2(1+a^2-2a\cos(\tau))^{3/2}} \\
& + \frac{a e_0'^2 \mu \cos(\tau)}{2(1+a^2-2a\cos(\tau))^{3/2}} - \frac{\mu}{(1+a^2-2a\cos(\tau))^{1/2}} + \frac{9 a^2 e^2 \mu \cos(2\tau)}{8(1+a^2-2a\cos(\tau))^{5/2}} \\
& - \frac{9 a^2 e_0'^2 \mu \cos(2\tau)}{8(1+a^2-2a\cos(\tau))^{5/2}} - \frac{27 a^2 e e'_0 \mu \cos(\beta + \tau)}{8(1+a^2-2a\cos(\tau))^{5/2}},
\end{aligned}$$

where $a = (x+1)^2$ and $e = \sqrt{1 - \left(\frac{y}{x+1} + 1\right)^2}$.

6.2 Form of the function H_b

Neglecting $\mathcal{O}(x)$ terms, and setting $b_0 = 2 - 2 \cos \tau$, $e_{p,0} = \sqrt{2(Y_f - Y_p)}$, the functions $\mathcal{F}^{(0)}$ and $\mathcal{F}^{(1)}$ of Eq.(27), up to second order in $e_{p,0}$ and e' , are analyzed in trigonometric terms in the angles τ , ϕ_f , and ϕ , as follows:

$$< \mathcal{F}^{(0)} >$$

Constant	$-1 + \frac{1}{b_0^{1/2}} + \frac{1}{b_0^{3/2}} \left(-\frac{3e'^2}{8} - \frac{3e_{p,0}^2}{4} \right) + \frac{1}{b_0^{5/2}} \left(3e'^2 + \frac{21e_{p,0}^2}{8} \right)$	
$\cos \tau$	$-1 + \frac{e_{p,0}^2}{2} + e'^2 + \frac{1}{b_0^{3/2}} \left(-e'^2 - \frac{e_{p,0}^2}{2} \right) + \frac{1}{b_0^{5/2}} \left(-\frac{27e'^2}{16} - \frac{3e_{p,0}^2}{2} \right)$	$\sin \tau$
$\cos 2\tau$	$-\frac{e'^2}{2} + \frac{1}{b_0^{3/2}} \left(\frac{e'^2}{8} \right) + \frac{1}{b_0^{5/2}} \left(-\frac{3e'^2}{2} - \frac{9e_{p,0}^2}{8} \right)$	$\sin 2\tau$
$\cos 3\tau$	$+\frac{1}{b_0^{5/2}} \left(\frac{3e'^2}{16} \right)$	$\sin 3\tau$

$$\tilde{\mathcal{F}}^{(0)} = \mathcal{F}^{(0)} - < \mathcal{F}^{(0)} >$$

$\cos(\phi_f)$	$\frac{3e_{p,0}}{2} + \frac{1}{b_0^{3/2}} \left(-\frac{3e_{p,0}}{2} \right)$	$\cos(\phi_f + \tau)$	$-e_{p,0} + \frac{1}{b_0^{3/2}} (e_{p,0})$
$\cos(\phi_f + 2\tau)$	$-\frac{e_{p,0}}{2} + \frac{1}{b_0^{3/2}} \left(\frac{e_{p,0}}{2} \right)$	$\cos(2\phi_f)$	$\frac{1}{b_0^{5/2}} \left(\frac{27e_{p,0}^2}{16} \right)$
$\cos(2\phi_f + \tau)$	$-\frac{e_{p,0}^2}{8} + \frac{1}{b_0^{3/2}} \left(\frac{e_{p,0}^2}{8} \right) + \frac{1}{b_0^{5/2}} \left(-\frac{9e_{p,0}^2}{4} \right)$	$\cos(2\phi_f + 2\tau)$	$-e_{p,0}^2 + \frac{1}{b_0^{3/2}} \left(\frac{e_{p,0}^2}{4} \right) + \frac{1}{b_0^{5/2}} \left(-\frac{3e_{p,0}^2}{8} \right)$
$\cos(2\phi_f + 3\tau)$	$-\frac{3e_{p,0}^2}{8} + \frac{1}{b_0^{3/2}} \left(\frac{3e_{p,0}^2}{8} \right) + \frac{1}{b_0^{5/2}} \left(\frac{3e_{p,0}^2}{4} \right)$	$\cos(2\phi_f + 4\tau)$	$\frac{1}{b_0^{5/2}} \left(\frac{3e_{p,0}^2}{16} \right)$

$$< \mathcal{F}^{(1)} >$$

$\cos(\phi)$	$+\frac{1}{b_0^{3/2}} \left(\frac{3e_{p,0}e'}{2} \right) + \frac{1}{b_0^{5/2}} \left(\frac{-15e_{p,0}e'}{8} \right)$	$\cos(\tau - \phi)$	$\frac{e_{p,0}e'}{4} + \frac{1}{b_0^{3/2}} \left(\frac{-e_{p,0}e'}{4} \right) + \frac{1}{b_0^{5/2}} \left(\frac{-3e_{p,0}e'}{2} \right)$
$\cos(\tau + \phi)$	$\frac{e_{p,0}e'}{4} + \frac{1}{b_0^{3/2}} \left(\frac{-e_{p,0}e'}{4} \right) + \frac{1}{b_0^{5/2}} \left(\frac{21e_{p,0}e'}{8} \right)$	$\cos(2\tau - \phi)$	$-e_{p,0}e' + \frac{1}{b_0^{3/2}} \left(\frac{e_{p,0}e'}{4} \right) + \frac{1}{b_0^{5/2}} \left(\frac{15e_{p,0}e'}{16} \right)$
$\cos(2\tau + \phi)$	$+\frac{1}{b_0^{5/2}} \left(-\frac{9e_{p,0}e'}{16} \right)$	$\cos(3\tau - \phi)$	$+\frac{1}{b_0^{5/2}} \left(\frac{3e_{p,0}e'}{8} \right)$
$\sin(\phi)$	$+\frac{1}{b_0^{3/2}} \left(-\frac{3\sqrt{3}e_{p,0}e'}{4} \right) + \frac{1}{b_0^{5/2}} \left(\frac{21\sqrt{3}e_{p,0}e'}{8} \right)$	$\sin(\tau - \phi)$	$-\frac{\sqrt{3}e_{p,0}e'}{4} + \frac{1}{b_0^{3/2}} \left(\frac{\sqrt{3}e_{p,0}e'}{4} \right) + \frac{1}{b_0^{5/2}} \left(\frac{3\sqrt{3}e_{p,0}e'}{4} \right)$
$\sin(\tau + \phi)$	$\frac{\sqrt{3}e_{p,0}e'}{4} + \frac{1}{b_0^{3/2}} \left(-\frac{\sqrt{3}e_{p,0}e'}{4} \right) + \frac{1}{b_0^{5/2}} \left(-\frac{3\sqrt{3}e_{p,0}e'}{4} \right)$	$\sin(2\tau - \phi)$	$+\frac{1}{b_0^{5/2}} \left(\frac{9\sqrt{3}e_{p,0}e'}{16} \right)$
$\sin(2\tau + \phi)$	$+\frac{1}{b_0^{5/2}} \left(-\frac{9\sqrt{3}e_{p,0}e'}{16} \right)$		

$$\tilde{\mathcal{F}}^{(1)} = \mathcal{F}^{(1)} - \langle \mathcal{F}^{(1)} \rangle$$

$\cos(\phi_f - \tau + \phi)$	$-2e' + \frac{1}{b_0^{3/2}} \left(\frac{e'}{2} \right)$	$\cos(\phi_f + \phi)$	$\frac{3e'}{4} + \frac{1}{b_0^{3/2}} \left(\frac{e'}{4} \right)$
$\cos(\phi_f + \tau + \phi)$	$-\frac{e'}{2} + \frac{1}{b_0^{3/2}} (-e')$	$\cos(\phi_f + 2\tau + \phi)$	$-\frac{e'}{4} + \frac{1}{b_0^{3/2}} \left(\frac{e'}{4} \right)$
$\cos(2\phi_f - 2\tau + 2\phi)$	$+\frac{1}{b_0^{5/2}} \left(\frac{3e'^2}{16} \right)$	$\cos(2\phi_f - \tau + \phi)$	$+\frac{1}{b_0^{5/2}} \left(-\frac{9e_{p,0}e'}{8} \right)$
$\cos(2\phi_f - \tau + 2\phi)$	$-\frac{27e'^2}{8} + \frac{1}{b_0^{3/2}} \left(\frac{3e'^2}{8} \right) + \frac{1}{b_0^{5/2}} \left(\frac{3e'^2}{16} \right)$	$\cos(2\phi_f + \phi)$	$3e_{p,0}e' + \frac{1}{b_0^{3/2}} \left(-\frac{3e_{p,0}e'}{4} \right) + \frac{1}{b_0^{5/2}} \left(\frac{3e_{p,0}e'}{16} \right)$
$\cos(2\phi_f + 2\phi)$	$\frac{3e'^2}{2} + \frac{1}{b_0^{3/2}} \left(-\frac{e'^2}{8} \right) + \frac{1}{b_0^{5/2}} \left(-\frac{63e'^2}{32} \right)$	$\cos(2\phi_f + \tau + \phi)$	$-\frac{e_{p,0}e'}{8} + \frac{1}{b_0^{3/2}} \left(\frac{e_{p,0}e'}{8} \right) + \frac{1}{b_0^{5/2}} (3e_{p,0}e')$
$\cos(2\phi_f + \tau + 2\phi)$	$-\frac{e'^2}{16} + \frac{1}{b_0^{3/2}} \left(\frac{e'^2}{16} \right) + \frac{1}{b_0^{5/2}} \left(\frac{3e'^2}{2} \right)$	$\cos(2\phi_f + 2\tau + \phi)$	$-e_{p,0}e' + \frac{1}{b_0^{3/2}} \left(-\frac{e_{p,0}e'}{2} \right) + \frac{1}{b_0^{5/2}} \left(\frac{-15e_{p,0}e'}{8} \right)$
$\cos(2\phi_f + 2\tau + 2\phi)$	$\frac{e'^2}{2} + \frac{1}{b_0^{3/2}} \left(-\frac{e'^2}{2} \right) + \frac{1}{b_0^{5/2}} \left(\frac{9e'^2}{8} \right)$	$\cos(2\phi_f + 3\tau + \phi)$	$-\frac{3e_{p,0}e'}{8} + \frac{1}{b_0^{3/2}} \left(\frac{3e_{p,0}e'}{8} \right) + \frac{1}{b_0^{5/2}} \left(-\frac{3e_{p,0}e'}{8} \right)$
$\cos(2\phi_f + 3\tau + 2\phi)$	$\frac{3e'^2}{16} + \frac{1}{b_0^{3/2}} \left(-\frac{3e'^2}{16} \right) + \frac{1}{b_0^{5/2}} \left(-\frac{15e'^2}{16} \right)$	$\cos(2\phi_f + 4\tau + \phi)$	$+\frac{1}{b_0^{5/2}} \left(\frac{3e_{p,0}e'}{16} \right)$
$\cos(2\phi_f + 4\tau + 2\phi)$	$+\frac{1}{b_0^{5/2}} \left(-\frac{3e'^2}{32} \right)$	$\sin(\phi_f + \phi)$	$\frac{3\sqrt{3}e'}{4} + \frac{1}{b_0^{3/2}} \left(-\frac{3\sqrt{3}e'}{4} \right)$
$\sin(\phi_f + \tau + \phi)$	$-\frac{\sqrt{3}e'}{2} + \frac{1}{b_0^{3/2}} \left(\frac{\sqrt{3}e'}{2} \right)$	$\sin(\phi_f + 2\tau + \phi)$	$-\frac{\sqrt{3}e'}{4} + \frac{1}{b_0^{3/2}} \left(\frac{\sqrt{3}e'}{4} \right)$
$\sin(2\phi_f - \tau + 2\phi)$	$+\frac{1}{b_0^{5/2}} \left(-\frac{9\sqrt{3}e'^2}{16} \right)$	$\sin(2\phi_f + \phi)$	$+\frac{1}{b_0^{5/2}} \left(\frac{27\sqrt{3}e_{p,0}e'}{16} \right)$
$\sin(2\phi_f + 2\phi)$	$\frac{3\sqrt{3}e'^2}{2} + \frac{1}{b_0^{3/2}} \left(-\frac{3\sqrt{3}e'^2}{8} \right) + \frac{1}{b_0^{5/2}} \left(\frac{3\sqrt{3}e'^2}{32} \right)$	$\sin(2\phi_f + \tau + \phi)$	$-\frac{\sqrt{3}e_{p,0}e'}{8} + \frac{1}{b_0^{3/2}} \left(\frac{\sqrt{3}e_{p,0}e'}{8} \right) + \frac{1}{b_0^{5/2}} \left(-\frac{9\sqrt{3}e_{p,0}e'}{4} \right)$
$\sin(2\phi_f + \tau + 2\phi)$	$-\frac{\sqrt{3}e'^2}{16} + \frac{1}{b_0^{3/2}} \left(\frac{\sqrt{3}e'^2}{16} \right) + \frac{1}{b_0^{5/2}} \left(\frac{3\sqrt{3}e'^2}{2} \right)$	$\sin(2\phi_f + 2\tau + \phi)$	$-\sqrt{3}e_{p,0}e' + \frac{1}{b_0^{3/2}} \left(\frac{\sqrt{3}e_{p,0}e'}{4} \right) + \frac{1}{b_0^{5/2}} \left(-\frac{3\sqrt{3}e_{p,0}e'}{8} \right)$
$\sin(2\phi_f + 2\tau + 2\phi)$	$-\frac{\sqrt{3}e'^2}{2} + \frac{1}{b_0^{3/2}} \left(-\frac{\sqrt{3}e'^2}{4} \right) + \frac{1}{b_0^{5/2}} \left(-\frac{15\sqrt{3}e'^2}{16} \right)$	$\sin(2\phi_f + 3\tau + \phi)$	$-\frac{3\sqrt{3}e_{p,0}e'}{8} + \frac{1}{b_0^{3/2}} \left(\frac{3\sqrt{3}e_{p,0}e'}{8} \right) + \frac{1}{b_0^{5/2}} \left(\frac{3\sqrt{3}e_{p,0}e'}{4} \right)$
$\sin(2\phi_f + 3\tau + 2\phi)$	$-\frac{3\sqrt{3}e'^2}{16} + \frac{1}{b_0^{3/2}} \left(\frac{3\sqrt{3}e'^2}{16} \right) + \frac{1}{b_0^{5/2}} \left(-\frac{3\sqrt{3}e'^2}{16} \right)$	$\sin(2\phi_f + 4\tau + \phi)$	$\frac{1}{b_0^{5/2}} \left(\frac{3\sqrt{3}e_{p,0}e'}{16} \right)$
$\sin(2\phi_f + 4\tau + 2\phi)$	$\frac{1}{b_0^{5/2}} \left(\frac{3\sqrt{3}e'^2}{32} \right)$		